Are Mussels and Oysters Spectrally Distinct?

GELIAH A. GLORIA
Enschede, The Netherlands, February, 2013

ITC SUPERVISORS:
Valentijn Venus
Dr. A.G.Toxopeus

Are Mussels and Oysters Spectrally Distinct?

GELIAH A. GLORIA
Enschede, The Netherlands, February, 2013

Thesis submitted to the Faculty of Geo-Information Science and Earth Observation of the University of Twente in partial fulfilment of the requirements for the degree of Master of Science in Geo-information Science and Earth Observation.
Specialization: Natural Resource Management

ITC SUPERVISORS:
Valentijn Venus
Dr. A.G.Toxopeus

THESIS ASSESSMENT BOARD:
Prof. Dr. A.K. Skidmore (Chair, ITC)
Dr. N.M.J.A. Dankers (External Examiner, IMARES)

DISCLAIMER

This document describes work undertaken as part of a programme of study at the Faculty of Geo-Information Science and Earth Observation of the University of Twente. All views and opinions expressed therein remain the sole responsibility of the author, and do not necessarily represent those of the Faculty.

ABSTRACT

The spectral distinctness of blue mussels and Japanese oysters were investigated and were found to be unique. Absorption features characteristic to carbonates and to water were found in their spectra. The general shape of their spectra was similar, but statistically different wavelengths were found in the visible range, particularly between 350 to 455 nm. However, its discrimination in hyperspectral image endmembers such as the AHS because of lack of coincidence with the AHS spectral range. The use of other significant bands, particularly those resulting from the statistical testing of mussel and oyster with other benthic cover types (e.g., seaweed, cockle), may offer an alternative. The 600 to 700 nm range, or the red-edge region, may be used to discriminate among all benthic cover types.

The simulation of varying observation geometries was performed to determine how mussel and oyster spectra are affected by various viewing and illumination angles. The results showed that the mussel and oyster spectra remain distinct, although their reflectance values were affected as the viewing angle and solar azimuth angle increased.

The image quality of the AHS was assessed to test its potential to detect mussel and oyster spectra. However, the radiometric, geometric, and atmospheric properties were found to be insufficient to map the shellfish spectra. Moreover, the statistically significant bands between 350-455 nm did not coincide with the AHS image.

Due to limited time, the recommendations of this study include further statistical analysis on the mussel and oyster spectra, particularly, through the J-M separability test. The use of a well-designed goniometer is also strongly recommended for the simulation of varying in-situ conditions. Finally, the use of the recalibrated AHS images or other hyperspectral images may deem more useful in detecting mussel and oyster spectra, provided that the image requirements for remotely sensing moisture-rich environments are satisfied.

In conclusion, further knowledge on the spectral distinctness of mussels and oysters is needed and further analytical steps should be made in order to answer whether mussels and oysters can be spectrally discriminated in hyperspectral imagery.

ACKNOWLEDGEMENTS

The journey to becoming a master of science would not have been possible without the Erasmus Mundus Mobility with Asia (EMMA) of the European Commission, who has granted me the scholarship to study in ITC, University of Twente. Kudos to EC for the continuous support for higher education and to ITC, for providing me an environment to develop my knowledge in Geo-information Science and Earth Observation for Natural Resources Management. This thesis is a testimony to what you have taught and to what I have learned.

The practice of science through research, small or big, is always an accomplishment of not one, but of many individuals.

To the Lord God Almighty, who has given me the skills and capacity to practice logical and critical thinking. My source of strength and courage to complete this thesis comes from You. Great is Thy faithfulness.

I graciously thank my first supervisor, Valentijn Venus, for his guidance and belief in my ability, although at times I could not show it. You have not trained me to become a researcher, but you have trained me to become a scientist.
To my second supervisor, Bert Toxopeus, I give my appreciation for his constant offer of mental and emotional support. You taught me that difficulty (in research) is good, or else it would be boring.

To Luc Boerboom and Iris van Duren who, in the pre-thesis stage, have assisted me in pursuing a research topic related to my areas of interest. To Henk Kloosterman, for taking time to listen and for the important realizations.

My deepest gratitude also goes to Henk Wilbrink, Boudewijn de Smeth, and Maria Fernanda Buitrago, for their reliable assistance during my laboratory work. Thank you for sticking out for me despite the prolonged unpleasant smell of my mussels and oysters.

Many thanks also to Thomas Groen, my “go-to” professor for any statistics-related questions. Thank you for always making time for other students like me. To Willem Niewenhuis, for his enthusiasm in helping me develop ENVI-IDL scripts. You are indeed Rock Steady.

Special thanks to Wim Bakker and Frank van Ruitenbeek, who were willing and kind enough to assist me in interpreting hyperspectral reflectance data and imagery. To the popular Job and Benno duo: what will I do without your material support? But really, thank you for your words of laughter and encouragement.

I am also indebted to Bruno Ens from Sovon, Norbert Dankers and Frouke Fey from IMARES, and Sindy Sterckx from VITO, who were responsible for providing me with all the remote sensing and GIS data that I needed. Thank you for your patience in responding to the flurry of emails. Thanks also to Kees Oosterbeek from Sovon and Sil Nieuwhof from NIOZ for their support during my fieldwork in Schiermonnikoog Island.

To my NRM-GEM classmates, it was a pleasure to have endured this 18-month long academic journey with you. Knowing that we will be parting ways in a few weeks’ time is bitter, yet sweet, as we are coming back home with the hope of seeing each other again somehow, in the future.

To my other ITC friends, thanks for the many fond memories and for the “Good Luck” wishes for the thesis. I would like to thank, in particular, Luz Adriana Guatame, who helped me make baby steps in interpreting hyperspectral reflectance data; and Nuno Cesár de Sá, who was integral in my completion of the statistical analysis.

To Coleen Carranza, for always spurring me to go forward when I was not motivated to do so. To Mr. Ethirkatchi who, in many ways, helped me learn important life lessons in school and outside. I cannot thank you enough.

Finally, to my parents and grandparents, who have worked so hard so I can have this privilege. All you ever wanted was for me to make the most out of what I have and who I am. This is for you.

TABLE OF CONTENTS

LIST OF TABLES

LIST OF FIGURES

1. Introduction

1.1. Background

Blue mussel beds (*Mytilus edulis*), are important biogenic structures that serve both as habitat and food source to other benthic organisms as well as water birds in the Wadden Sea ecosystem (Nehls et al., 2009). They are also an important resource for shellfish fishery for the Netherlands, Germany, and Denmark, the three countries bordering the Wadden Sea. Mussel beds have drastically declined in number and in size since the 1980s due to unregulated fishing, hence, management plans were put in place to regulate fishing activities and monitor the development of both intertidal and subtidal beds (Nehls et al., 2009). Concurrently, the introduced Japanese oysters (*Crassostrea gigas*) have successfully established themselves in the Wadden Sea (Wolff et al., 2010), and have already overgrown many mussel beds (TMAP, 2011). This raises concern in their potential impact on mussel bed development and thus, efforts have also been made to monitor it. Monitoring strategies, such as those employed by the Trilateral Monitoring Assessment Programme (TMAP), include the mapping of stable mussel beds using aerial photography and field surveys. Such mapping technique, however, only focuses on surveying parameters related to mussel beds (e.g., area, biomass, percentage cover) and, to a lesser degree, the invasive Japanese oysters (TMAP, 2011). Specifically, Japanese oysters have not been distinguished from or within mussel beds in aerial photos or through any other remote sensing method. It is in this context that the spectral distinctness of the blue mussel vs. the Japanese oyster are explored, as such distinctness could potentially yield discriminative ability of aforementioned and other benthic cover types using hyperspectral imagery. A more cost-effective and novel mapping technique based on such a premise would allow dual monitoring of native and invasive shellfish species in the Wadden Sea.

1.2. Japanese Oyster Invasion

The Japanese oyster (also called Pacific oyster) is one of 50 introduced (e.g., alien/invasive) algae and invertebrate species (Wolff et al., 2010), and one of 70 molluscan species (Reise et al., 2010) in the Wadden Sea. It was introduced to Northern Europe in the 1980s as an alternative oyster culture to the overfished native European oyster (*Ostrea edulis*) (Diederich, 2006). Their cultivation was a success, not only in known culture farms but also in the wild, as abiotic factors (e.g., ocean currents, warmer water temperatures) aided the natural dispersion and recruitment of oyster larvae (Nehls et al., 2009). Presently, the Japanese oyster can be found in all parts of the Wadden Sea, increasing steadily in size and in some cases, having equal or higher biomass than mussels, causing a change in the habitat structure of mussel beds (Nehls et al., 2009).

The successful establishment of Japanese oysters makes them a potential threat to the native blue mussels. In their settlement, young oysters attach themselves to existing hard substrates such as mussel beds. As a result, oysters become epibionts on mussels which they eventually overgrow and displace (Diederich, 2006). Oysters were also found to have survival and growth rates that are superior to that of mussels, thus, possibly restricting the habitat use of the latter, especially in the context of warmer summer water temperatures and severe winters (Diederich, 2006). Most importantly, Smaal et al. (2005) also discussed how a shift to a predominant oyster population can affect food availability for waterbirds. Waterbirds depending on intertidal mudflats have already been experiencing strong population declines since the 1980s (Laursen et al., 2010; van Roomen et al., 2012). A monitoring strategy for oysters is therefore needed and is in fact recommended that combined surveys for both mussel and oyster species be made (TMAP, 2011).

1.3. Current Blue Mussel Management Plans & Strategies

At present, all three states bordering the Wadden Sea have made efforts to “protect, conserve, and, where necessary, restore the Wadden Sea as a nature area” (Verbeeten, 1999, p. 7). Such endeavors are evident in the implementation of the Trilateral Cooperation on the Protection of the Wadden Sea, the OSPAR Commission, the European Union Water Framework Directive, and more recently, in the designation of the Wadden Sea as a UNESCO World Heritage Site (see References section for website pages) (Wolff et al., 2010). Monitoring of mussel beds per se, however, have been implemented at a country-by-country basis under the Trilateral Monitoring and Assessment Programme (TMAP). Country-based projects are also implemented, such

as the Dutch project “Mosselwad,” which provides scientific support for the construction and recovery of stable mussel beds.

In TMAP surveys of intertidal blue mussels, the mandatory parameters measured are: (1) area (border/contour) and distribution, biomass (tons fresh weight), and coverage (percentage covered by mussels) (TMAP, 2011). Japanese oysters often occur together with mussels in the same bed and are therefore sampled together in blue mussel surveys. As a result, rough estimates of their biomass have been made (Nehls et al., 2009). Although survey methods have been developed, oyster beds have not yet been monitored as extensively as mussel beds (Nehls et al., 2009). With the growing concern for the invasion of oysters in the native territory of mussels rises a pressing need to continuously monitor their distribution vis-à-vis the mussels.

1.4. Research Problem

1.4.1. Monitoring Strategies using Remote Sensing

Remote sensing applications primarily dedicated to mapping and monitoring mussel beds in the Wadden Sea have often relied on the visual interpretation of aerial photography (Millat & Herlyn, 1999; Stoddard, 2003; Herlyn, 2005; Herlyn et al., 2008; Fey et al., 2009). For validation, results are compared with field data. Experience or a strong background of the study area is also beneficial for successful and accurate mapping (Stoddard, 2003). Series of aerial photographs of certain parts of the Wadden Sea were made available since the 1960s (Millat & Herlyn, 1999), thereby adding to the benefit of its use not only for documentation of mussel beds but also for habitat modeling (Herlyn et al., 2008). In fact, the TMAP considers remote sensing by aerial photography as indispensable (Herlyn, 2005). However, there remains a need to develop a standard method for aerial photograph analysis of mussel beds (Stoddard, 2003). Brockmann and Stelzer (2008) believe that this method, due to its manual nature, lacks objectivity and therefore lack repeatability. Moreover, aerial photos can only distinguish the *location and area* (borders/contours) of the mussel beds and on a lesser degree, mussel bed cover and proportion, depending on the aerial photo scale (Herlyn, 2005). Distinguishing Japanese oysters within mussel beds cannot be done on aerial photos (TMAP, 2011). In fact, distinguishing Japanese oysters from blue mussels has never been accomplished remotely and has only been established through field surveys.

1.4.2. General Objective

The aim of this research is to determine whether blue mussels and Japanese oysters are spectrally distinct and if such distinctness could be used to discriminate between the two shellfish species in airborne hyperspectral imagery. In addition, the requirements of hyperspectral imagery in detecting such species will be investigated. Overall, the goal is to contribute to the knowledge of spectroscopy in order to evaluate monitoring strategies for the shellfish species in the protected Wadden Sea.

1.4.3. Specific Objectives

a. To investigate the spectral distinctness of mussels and oysters in a controlled environment
b. To discriminate between mussel and oyster spectral reflectance
c. To determine how spectra of mussels and oysters are affected by varying observation geometries
d. To test the potential of in-situ hyperspectral imagery in detecting shellfish spectra

1.4.4. Research Questions

a. Are blue mussels spectrally distinct from Japanese oysters, based on their shells?
b. Can diagnostic absorption features in mussel and oyster shell spectra be used for discriminating corresponding image endmembers of a hyperspectral image?
c. Do spectra of mussels and oysters remain distinct under varying observation geometries?
d. What are the image requirements (radiometric, atmospheric, and geometric quality) for hyperspectral (and potentially, multispectral) remote sensing to be successful in mapping oysters and mussels?

1.4.5. Research Hypothesis

Ha^1: The different physicochemical properties of the mussel and oyster shells cause them to be spectrally unique from each other.
Ha^2: Unique diagnostic absorption features in the visible and shortwave infrared region can be used to discriminate mussels and oysters from the corresponding image endmembers extracted from the AHS.
Ha^3: The spectral distinctness of mussels and oysters is robust to varying sensor viewing angles and illumination angles.
Ha^4: The radiometric, atmospheric, and geometric properties of AHS as well as other hyperspectral sensors (i.e., EnMap) and potentially also multispectral sensors (i.e., MERIS, Sentinel-2) are sufficient for detecting mussels and oysters based on their spectral properties.

2. Literature Review

2.1. Mussels and Oysters

2.1.1. Ecological Role in the Wadden Sea

The Wadden Sea, comprising the southeastern portion of the North Sea and bordering the coasts of Denmark, Germany, and the Netherlands, is the largest intertidal zone in the temperate region of the world (Reise et al., 2010). This tidal wetland has a 4,500 km^2 expanse of sand and mudflats that receive a constant flow of nutrients both from oceanic and fluvial sources, making it an important habitat for soft-bottom communities and other organisms (Eriksson et al., 2010; Reise et al., 2010). In particular, the tidal flats are home to the blue mussels (*Mytilus edulis*), a bivalve or shellfish species often used to describe the ecology of the Wadden Sea (Baird et al., 2007; van der Graaf et al., 2009). Blue mussels are suspension feeders that feed on organic particles from the water column (Newell, 1989), simultaneously filtrating up to five liters of water per hour (Nordsieck, n.d.). They are also ecosystem engineers (Eriksson et al., 2010). By attaching themselves to each other and to the substrate by means of their byssal threads, they form reefs or mussel beds that stabilize bottom sediments through mud and shell accumulation (Ehlers, 1988; Reise et al., 2010). Mussel beds, with their high biomass densities, in turn act as food source to birds, crabs, and starfish (Brinkman et al., 2002). Blue mussels perform a crucial role in the ecosystem by connecting the primary producers to the higher trophic levels of the food web (van der Graaf et al., 2009), influencing the sediment properties of its environment (Eriksson et al., 2010), and serving as indicators of the biological quality of coastal waters (Büttger et al., 2010).

Blue mussels are not the only shellfish in the Wadden Sea. Reise et al. (2010) records 69 other molluscan species, including the common cockle (*Cerastoderma edule*) and the sand gaper (*Mya arenaria*). Aside from the native species, at least 50 introduced algae and invertebrate species have successfully established in the Wadden Sea (Wolff et al., 2010), ten of which are known to have settled on mussel beds (Nehls et al., 2009). Perhaps the most important of these is the Japanese oyster/Pacific oyster (*Crassostrea gigas*), whose potential impact on the blue mussel population has already been discussed in Chapter 1. The rate of survival of the former seems better than the latter, as it can filtrate up to 30 liters of water (Diederich, 2006), have better reproduction success, and have no natural predators. These facts suggest that Japanese oysters can almost replace the ecological function of blue mussels in the intertidal Wadden Sea (Nehls et al., 2009).

Nevertheless, it remains noteworthy to stress the importance of the native blue mussels, especially their role as food source. In particular is the dependence of several migratory waterbird species on mussel beds. The Common Eider (*Somateria mollissima*) and the Eurasian Oystercatcher (*Haematopus ostralegus*) are two examples of shellfish-feeding birds which are both experiencing strong declines in population since the 1980s (Laursen et al., 2010; van Roomen et al., 2012). Many studies have attributed this decline to intensive mussel and cockle fishery, among other causes (Ens et al., 2004; Ens, 2006; Laursen et al., 2010). Likewise, unregulated mussel fisheries in the 1980s have resulted in overfished shellfish stocks and have even been linked with the near-disappearance of intertidal mussel beds (Ens et al., 2004). As a remedy, management plans were established to protect mussels and other bivalves from overexploitation (van Roomen et al., 2012). Beginning in the 1990s, substantial areas of intertidal mussel beds were permanently closed to fishing and, coupled with consistent monitoring, thereby promoted their conservation value of mussel beds (Nehls et al., 2009).

2.1.2. Physico-Chemical Characteristics

There are obvious differences in the shells of the blue mussel and the Japanese oyster (see Figure 1). The blue mussel shell has fine concentric lines and can be dark blue, black, or brown, in color (Newell, 1989). The Japanese oyster shell, on the other hand, is whitish with purple streaks and extensively grooved (Pauley et al., 1988). The mussel shell is smoother compared to the oyster shell, which is rough and more variable. However, barnacles and algae are often attached to the shells of both mussels and oysters, thereby

contributing to the variability in smoothness. Mussel shells are shorter (7-10 cm.) than oyster shells (10-25 cm.) (Pauley et al., 1988; Newell, 1989).

Figure 1. Blue Mussel (*Mytilus edulis*) (Left) and Japanese Oyster (*Crassostrea gigas*) (Right)
Source: (Tucker, 2009)

The shells of mollusks like mussels and oysters are composed of three layers (see Figure 2). The first layer is called the *periostracum*, the external layer or skin which is organic, consisting mainly of a keratin protein called conchiolin. The second and third layer (*ostracum* and *hypostracum*) are both made of calcium carbonate ($CaCO_3$) and may either be of calcite or aragonite form (Nordsieck, n.d.). The formation of either calcite or aragonite, or the dominance of one polymorph over the other depends on the species and its environmental conditions (e.g., saltwater or freshwater)(Farson, n.d.). For the case of remotely distinguishing one species from the other, only the first and second layers (periostracum and ostracum) of the shell are of interest, as the hypostracum is already found on the interior part of the shell (Farson, n.d.).

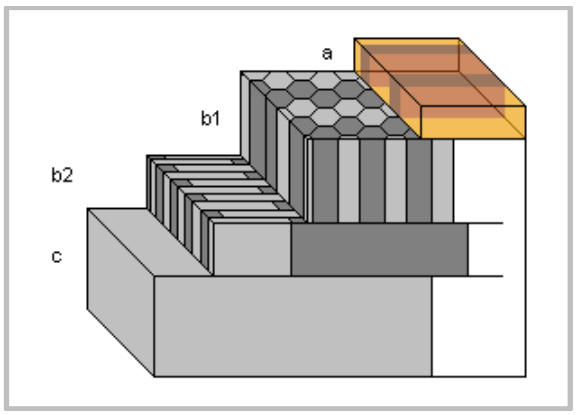

Figure 2. The layers of a mollusk shell.
a: Periostracum;
b: Ostracum:
b1: Prism layer;
b2: Plate layer;
c: Hypostracum
Source: (Nordsieck, n.d.)

The physico-chemical properties of the mussel and oyster shell discussed above are important, as these indicate what kind of spectra they may exhibit and why. The spectral characteristics of the two species are discussed in the next section.

2.1.3. Spectral Characteristics

In order to assess whether hyperspectral data can distinguish between a mussel and oyster shell, an understanding of the "behavior" of their spectra is first required. This can be done through spectroscopy, which is defined as "the science of measuring the emission and absorption of different wavelengths (spectra) of visible and non-visible light" (National Research Council Canada, 2005). In spectroscopy, questions such as "What characteristic absorption/reflectance features are evident?" and "To what chemical or physical property of the shell can these be attributed?" must be kept in mind. Thus, the underlying theory is that given the differences in the shell properties of the blue mussel and the Japanese oyster, at certain wavelengths they will exhibit characteristic absorption/reflectance, hence, resulting in distinct spectral signatures. For example, it is easy to assume that the oyster will have higher reflectance than the mussel, since its shell color is white and will therefore appear brighter than the blue mussel shell. In terms of chemical composition, both shells are the same ($CaCO_3$) but may vary in amounts and may contain other trace elements such as magnesium and

iron ("The Shell," 2006). In fact, the calcium carbonate structure of shells has been studied since the 1950s, especially through infrared spectroscopy (Adler & Kerr, 1962; Compere & Bates, 1973). The shells are also expected to exhibit similar absorption features with pure minerals like calcite and aragonite. In particular, the absorption band positions at 2.3 µm and 2.5 µm in the near infrared region (NIR) and 11-11.5 µm in the thermal infrared region (TIR) are characteristic of carbonate minerals, brought about by vibrational processes of the carbonate ion (Adler & Kerr, 1962) (see Figure 3). To summarize, if differences in mussel and oyster shell spectra are found to be distinct, can their spectral signatures then be used as a discriminator for mapping using hyperspectral imagery?

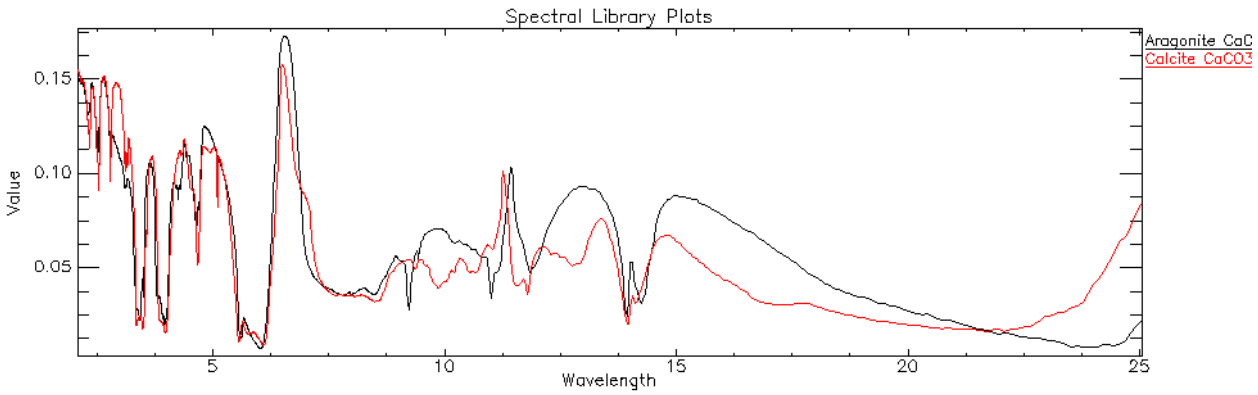

Figure 3. Aragonite and calcite ($CaCO_3$) spectra of pure minerals in the infrared region (2-25 µm).
Source: John Hopkins University Spectral Library accessible as minerals.sli in ENVI 4.8

2.2. Hyperspectral Remote Sensing of Coastal Waters

2.2.1. Discriminating Power of Hyperspectral Data

Hyperspectral sensors (also known as imaging spectrometers) have the ability to measure reflectance of surface properties in a large number of continuous, narrow spectral bands. Hyperspectral data can contain over a hundred bands encompassing the visible, near-infrared, mid-infrared, and thermal infrared regions of the electromagnetic spectrum. This advantage over the fewer and broader band multispectral scanners gives them the better potential to discriminate between the spectra of blue mussels, Japanese oysters, and other benthic cover types.

The ability of hyperspectral data in discriminating on a species level has been explored, especially in the field of vegetation, where tree species were discriminated on the leaf level (Vaiphasa, 2006; Wang & Sousa, 2009; Kumar et al., 2010; Ullah et al., 2012). In coastal applications, hyperspectral remote sensing has been used in mapping benthic communities (e.g., algae, corals) and substrates in various in-situ conditions, with promising results (Hochberg & Atkinson, 2000; Vahtmäe et al., 2006; Vahtmäe & Kutser, 2007; Casal et al., 2011; Leiper et al., 2012). Ibrahim et al. (2009) also displayed the success of unsupervised classification of sediments on a hyperspectral image of a Belgian estuary. In the Wadden Sea area, (Schmidt et al., 2004) demonstrated that 19 vegetation types could be classified better (66%) in a hyperspectral image aided with an expert system as compared to aerial photographs (43%).

2.2.2. Remote Sensing of Shallow Coastal Waters

Further efforts in monitoring have also been done using remote sensing applications. Remote sensing offers an alternative for more cost-efficient mapping and monitoring, with advantages of data integration in a wider spatial context (Brockmann & Stelzer, 2008; Ruddick et al., 2008). It is especially useful for monitoring intertidal mudflats, which are often inaccessible and labor-intensive and time-consuming to survey otherwise in a long-term basis (Hennig et al., 2007; Brockmann & Stelzer, 2008). To illustrate, the book *Remote Sensing of the European Seas* edited by Barale and Gade (2008) includes two sections on the applications of optical remote sensing covering the Wadden Sea. These sections, authored by Brockmann and Stelzer (2008) and Ruddick et al. (2008), review the mapping efforts done to monitor various parameters of intertidal flats

including sediment type, nutrient concentrations, vegetation, as well as mussel beds. Other studies have also documented the ability of optical remote sensors in mapping the same (Schmidt et al., 2004; Ruddick et al., 2008; Fey et al., 2009).

A demonstration of its use is shown in Hennig et al. (2007), wherein a hyperspectral image of sub-meter spatial resolution yielded a classification of the dominant intertidal biotope structures in Helgoland. van der Wal et al. (2008) also illustrated the usefulness of a temporal series of hyperspectral imagery in predicting the distribution of macrobenthos in a Dutch coastal estuary.

2.2.3. Challenges in Remote Sensing of Intertidal Areas

Despite of the many demonstrations on the use of hyperspectral imagery in coastal applications, remote sensing challenges inherent to these dynamic ecosystems remain. To illustrate, Brockmann and Stelzer (2008) itemizes four main issues that need to be accounted for when mapping intertidal areas using optical remote sensing: (1) spatial heterogeneity; (2) relation between biological and morphological features and the surface reflectance spectrum; (3) water coverage of the surface; and (4) atmospheric effects. In relation, Hommersom et al. (2010) discusses how substances (e.g., chlorophyll, dissolved organic matter) and processes (e.g., seasonal and tidal variations) contribute to the optical heterogeneity of intertidal areas. For example, chlorophyll concentrations are lowest during winter and highest during spring. High chlorophyll concentrations can lead to low penetration depth of sunlight (Hommersom et al., 2010). Therefore, if a hyperspectral sensor was to acquire images over an area in the Wadden Sea that has high chlorophyll concentrations (e.g., Dutch part) and during summer where chlorophyll is at its maximum, radiance data may be affected and certain water quality algorithms may need to be applied. Moreover, in classifying surface types, sub-pixel heterogeneity must be expected, regardless of pixel size. The viewing geometry and spatial, spectral, and radiometric resolutions of the sensor also need to be accounted for. These varying in-situ conditions should not be ignored especially when using hyperspectral systems which, with their large data volume, consequently require high data processing effort. Such data processing is not straightforward hence, choosing the appropriate image processing algorithms is vital in accomplishing optimal results in the extraction, analysis, and classification of hyperspectral data (Vaiphasa, 2006).

As much as these challenges exist, hyperspectral imagery still has the power to “discriminate among earth surface features that have diagnostic absorption and reflection characteristics over narrow wavelength intervals” (Lillesand et al., 2004, pp. 384-385). Furthermore, hyperspectral imagery are becoming increasingly available and affordable (Schill et al., 2006). These reasons encourage the pursuit of exploring the use of hyperspectral data for discriminating among benthic cover types in dynamic coastal systems based on their spectral distinctness. In doing so, a new (and possibly) and cost-effective mapping technique is proposed, which could effectively monitor both native and invasive species in the Wadden Sea.

3. Methods & Materials

3.1. Study Area

The chosen area of study are the intertidal mudflats south of Ameland and Schiermonnikoog, two of the five barrier islands of the Dutch Wadden Sea (see Figure 4). These mudflats contain around 345 ha of stable (mature) mussel beds (Fey et al., 2009).

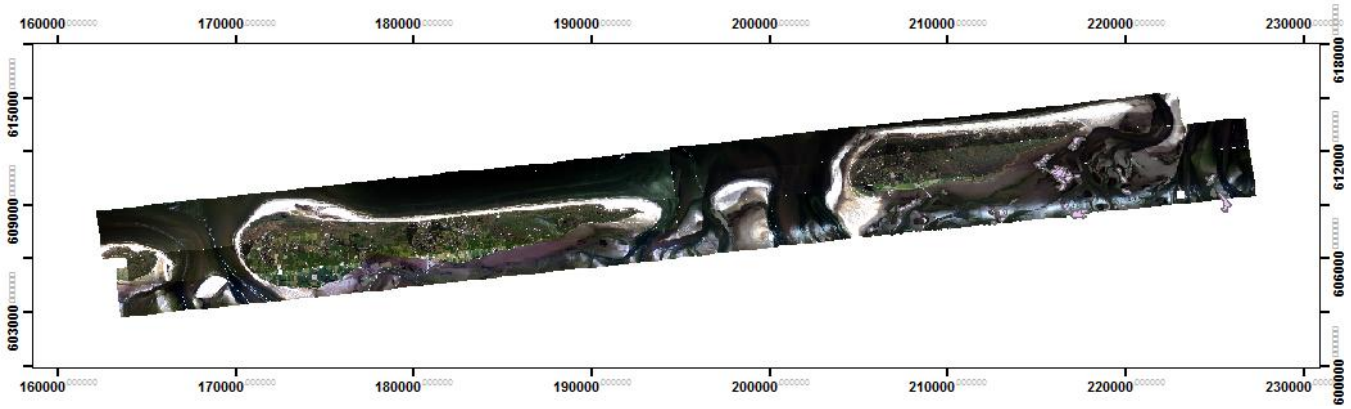

Figure 4. Study area of Ameland (Left) and Schiermonnikoog (Right)

3.2. Flow of the Research

The implementation of the research is done in three stages (see Figure 5). Stage 1 encompasses the investigation of benthic cover spectra while Stage 2 is devoted to the simulation of varying in-situ conditions. Both analyses fall under laboratory measurements. Stage 3 is on the analysis of the image quality of the hyperspectral datasets. The methods and materials of each stage are discussed in Chapter 3. The results and discussion are found in Chapter 4. Finally, the conclusion and recommendations are found in Chapter 5.

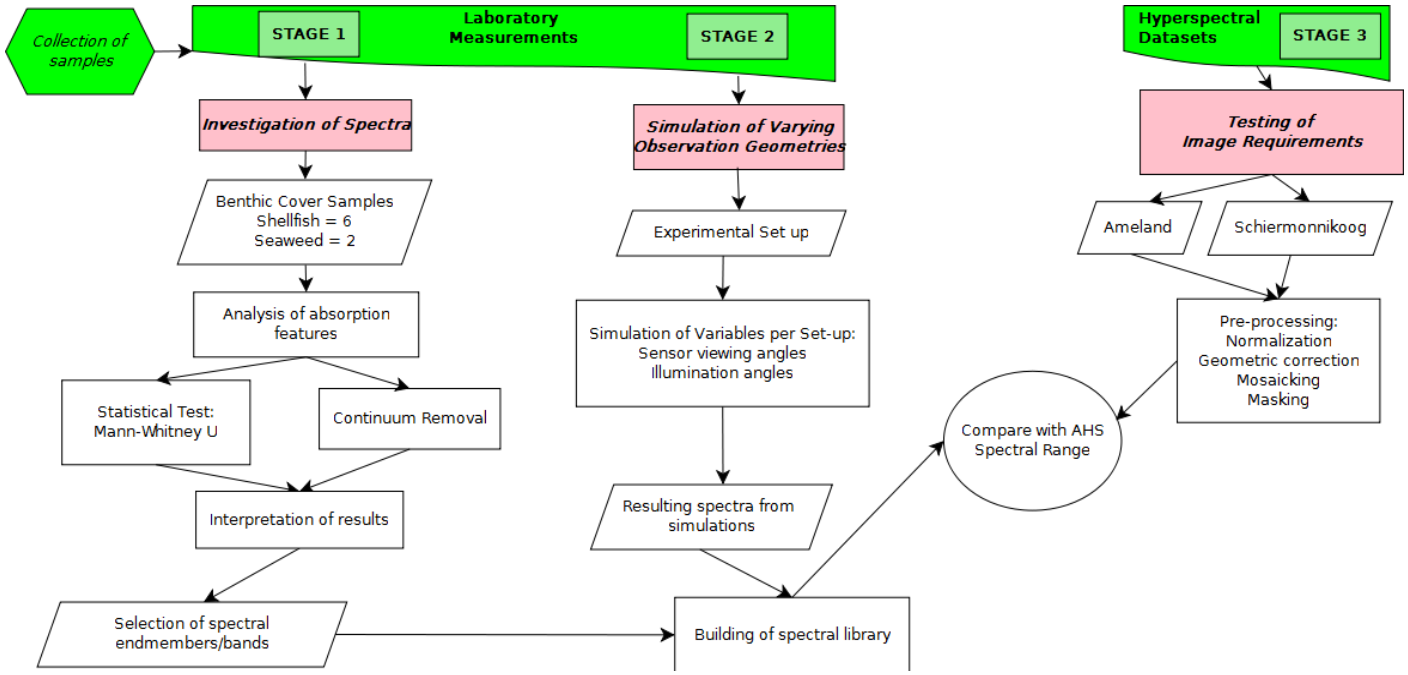

Figure 5. Research Flow

3.3. Investigating the Spectral Distinctness of Blue Mussels & Japanese Oysters

3.3.1. Collection of Samples

A fieldwork to the island of Schiermonnikoog took place on October 23-27, 2012. One of the purposes of the fieldwork was to collect samples of mussels and oysters for laboratory measurements. Seeing that there were other shellfish species and benthic cover present in the study area, samples of these were also collected. The samples collected were: 4 types of bivalves and 2 types of seaweed (See photos in Appendix A). A detailed description of the collected benthic cover is found in Table 1. Samples of mud, sand, and seawater were also collected for reference.

Table 1. Benthic Cover Samples Collected

Benthic Cover	Description	Condition
1. Blue Mussel *Mytilus edulis*	A. Smooth; dark blue to white in color B. Covered in barnacles	Empty shells as well as live mussels whose shells are still closed
2. Pacific Oyster *Crassostrea gigas*	A. Grooved; purple to white streaks B. Covered in barnacles	Empty shells as well as live oysters whose shells are still closed
3. Cockle *Cerastoderma edule*	A. Grooved; white to brownish yellow in color B. Covered in barnacles	Empty shells as well as live cockles whose shells are still closed
4. Razor shell *Ensis arcuatus*	Smooth; razor-shaped; reddish brown/purplish brown in color	Empty shells
5. Bladder Wrack *Fucus vesiculosus*	Branched; brown seaweed	Live
6. Green Hair Algae *Chaetomorpha spp.*	Thin and thread-like green seaweed	Live

3.3.2. Spectral Measurements

A spectroradiometer (FieldSpec Pro FR, Analytical Spectral Devices, Boulder, CO, USA) was used to measure the spectral reflectance of the samples. This instrument measures in the Visible to Short-Wave Infrared range (350-2500 nm) with a spectral resolution of 3 nm at 700 nm and 10 nm at both 1400 and 2100 nm. The 350-1000 nm (VNIR) range is sampled at 1.4 nm intervals while the 1000-2500 nm range is sampled at 2.2 nm intervals, while the entire 350-2500 nm range is resampled to 1 nm upon export to the computer. To allow for pure spectral measurements with negligible influence from the atmosphere and other sources of illumination, the FieldSpec contact probe was used. This ASD accessory is equipped with a field of view of 25^{o} and a cap with white interior that serves as white reference during calibration. The instrument was calibrated to produce a spectral average of 25 readings. The reader is directed to the FieldSpec User Manual (ASD Inc., 2008a) and the ViewSpec User Manual (ASD Inc., 2008b) for further reference to the instruments and software used.

The samples were first cleaned of sediments such as mud and sand. This was done to minimize the influence of mud and sand spectra to the spectra of the samples. A mini experiment done recently revealed that spectra of shells with epibionts have variations with the spectra from a smooth (clean) shell. Also, it was observed from the field that barnacles (a type of epibiont) were abundant on the surfaces of mussels, oysters, and cockles. For this reason, separate measurements were done for smooth shells and shells covered with barnacles. The following measurements were then made for:

(1) Mussel (smooth shell)
(2) Mussel_B (mussel covered with barnacles)
(3) Oyster (smooth shell)
(4) Oyster_B (oyster covered with barnacles)
(5) Cockle
(6) Razor
(7) Seaw_B (bladder wrack)
(8) Seaw_G (green hair algae)

All in all there were 6 shellfish types and 2 seaweed types measured. Each shell was measured five times with the ASD. Spectral measurements were also made on mud and sand samples. The recorded spectra, which were in radiance values, were then splice-corrected and converted to reflectance values. The benthic cover spectra will then be compared visually with the sediment spectra as well as with pure spectra of carbonates that are available from mineral spectral libraries in ENVI.

As a further step in analysis, the reflectance values were also applied with continuum removal, a waveform characterization technique commonly used in geological applications. Schmidt and Skidmore (2003, p. 95) provide a brief description of how continuum removal works:

> The continuum is a convex hull fitted over the top of a spectrum utilizing straight line segments that connect the local maxima. The convex hull can be thought of as the shape a rubber band would attain, if it were stretched over the reflectance spectrum. This means the number of contact points between convex hull and reflectance spectrum is minimized and they are connected by straight lines that do not cross the spectrum itself. Therefore, different reflectance spectra have a convex hull with contact points at different wavelength positions, depending on the shape and position of reflectance maxima.

In continuum removal, reflectance values are normalized to produce a curve with values between 0 to 1, emphasizing the location and depth of individual absorption features and isolating background signals (Schmidt & Skidmore, 2003). This method then provides better analysis of data comparisons and will likewise be applied to the spectra for further analysis on the statistical differences.

3.3.3. Band Selection

To investigate whether the mussel and oyster (and other benthic cover) have significant differences in their spectra, statistical tests need to be employed. Such methods, when applied to the reflectance spectra (VNIR-SWIR) of the benthic cover can identify which bands/wavelengths are statistically significant and would therefore be robust indicators for species discrimination.

A. Mann-Whitney U Statistical Test

The Mann-Whitney U Test was selected to statistically differentiate among the benthic cover spectra. This non-parametric test is more suited when assumptions of parametric tests cannot be met, such as the source population being normally distributed. It is also ideal for dealing with “dirty” data (data contains errors) (Venus et al., 2006) and small sample sizes, which is the case of the benthic cover reflectance spectra (each species or type was measured only 5 times). The Mann-Whitney U Test has then the following assumptions (Lowry, 2012, p. 2):

(1) The two samples are randomly and independently drawn;
(2) The dependent variable is intrinsically continuous;
(3) The measures within the two samples have the properties of at least an ordinal scale of measurement.

For this test, the null hypothesis is that there is no significant difference between the medians of reflectance for each measured wavelength between two samples. For this test, the number of benthic cover types was reduced to the following:

(1) Oyster
(2) Mussel
(3) Mussel_B
(4) Oyster_B
(5) Cockle
(6) Seaw_B

Since there are 6 benthic cover types, a total of 15 pairs are to be tested. The test was implemented using RStudio, using a customized script that employed the five measurements of each type and yielding a p-value for each pairing made. The reader is guided to the R documentation on using Mann-Whitney U Test for more detailed information (see "Wilcoxon rank sum and signed rank tests," n.d.).

The Mann-Whitney U is an inferential test that answers whether there is a statistically significant difference between two benthic cover spectra. If there is, the null hypothesis is rejected, and the alternative hypothesis will be true, wherein "the variance within two types is smaller than the variance between them" (van Til et al., 2004, p. 158). This means that bands where these differences occur and with which benthic cover pairs will be identified. The next step should then be to test the discriminative ability of these bands to discriminate between two given types. This is done by using a separability test such as the Jeffries-Matusita Distance.

B. Jeffries-Matusita Distance

The Jeffries-Matusita distance is a separability index that measures the distance between two or more distributions (University of Idaho, 2006). It gives the probability of how good a classifier (e.g., band) could be. It is often used in discriminating vegetation species (Schmidt & Skidmore, 2003; Vaiphasa, 2006; Ullah et al., 2012). The J-M distance is asymptotic to the value of 2, where 2 indicates the highest value of separability. The formula for J-M is given as:

$$J\text{-}M_{ub} = \sqrt{2(1-e^{-\alpha})}$$

$$\alpha = \frac{1}{8}(\boldsymbol{\mu}_u - \boldsymbol{\mu}_b)^T \left(\frac{\mathbf{C}_u + \mathbf{C}_b}{2}\right)^{-1} (\boldsymbol{\mu}_u - \boldsymbol{\mu}_b) + \frac{1}{2}\ln\left[\frac{\frac{1}{2}|\mathbf{C}_u + \mathbf{C}_b|}{\sqrt{|\mathbf{C}_u| \times |\mathbf{C}_b|}}\right]$$

Where,

u and *b* (i.e., classes 1 and 2) are the two signatures (classes) being compared,
$\mathbf{C_u}$ is the covariance matrix of signature u,
$\mathbf{m_u}$ is the mean vector of signature u,
T is the transposition function.

Figure 6. Formula for Jeffries-Matusita Distance
Source: (Smith, 2009, p.11)

3.4. Simulation of Varying Observation Geometries

3.4.1. Selection of Simulation Variables

Because of the dynamic nature of intertidal environments, variabilities in seasonal and even daily changes of mudflats need to be carefully considered when mapping benthic species. Moreover, remote sensing using optical airborne sensors such as the AHS also mean variability in the viewing geometry and illumination over the length of an image swath. The complexities of both the natural environment and the remote sensing system ultimately affect the spectra of benthic species and how they are obtained. There is, therefore, a need to investigate how their spectral reflectance is influenced by these variables. Given that there are ultimately many factors/variables that can be possibly modeled, the study will limit such variables to the following variables related to observation geometry:

(1) Viewing zenith angles (VZA) & viewing azimuth angles (VAA) of various sensors
(2) Solar zenith angles (SZA) & solar azimuth angles (SAA) of various times of the day & seasons of the year

Viewing zenith angle (VZA) is defined as the angle between the sensor and a line perpendicular to the Earth's surface at a given viewpoint (TeraScan, 2002, para. 1). Similarly, the illumination or the solar zenith angle (SZA) is the "angle between the sun and a line perpendicular to the Earth's surface" (TeraScan, 2002, para. 1). A relative angle called the viewing azimuth angle (VAA) for the sensor and the solar azimuth angle (SAA) for the sun is the angle between sun and sensor vectors "projected on a plane tangent to the Earth's surface" (TeraScan, 2002, para. 1). An illustrative example of these angles is provided in Figure 7.

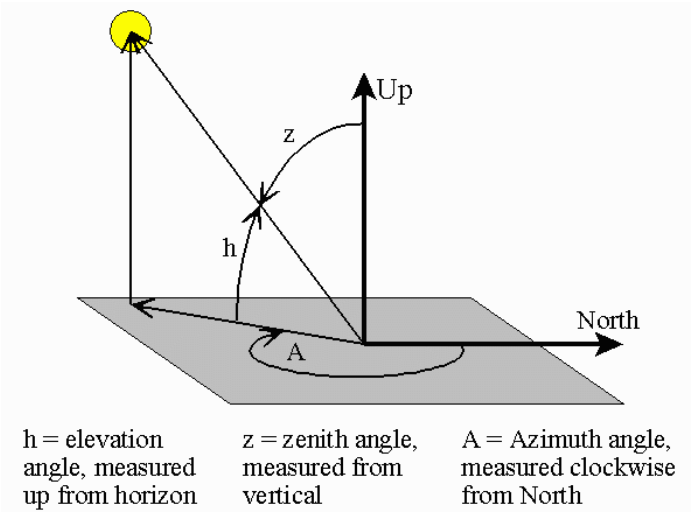

Figure 7. Azimuth, Elevation, and Zenith Angles

Source: (NOAA, n.d.)

In order to simulate the possible effects of sensor viewing geometry in acquiring shellfish spectral reflectance, information on their viewing geometry were obtained. This was done primarily to simulate the viewing geometry of the AHS sensor, whose image products were analyzed in this study. In the anticipation that other hyperspectral sensors as well as multispectral sensors would be potentially useful and more readily available in the future, a selection of sensors and their viewing geometry were included in the simulation (see Figure 8). Their spectral range and resolution are provided in Table 2.

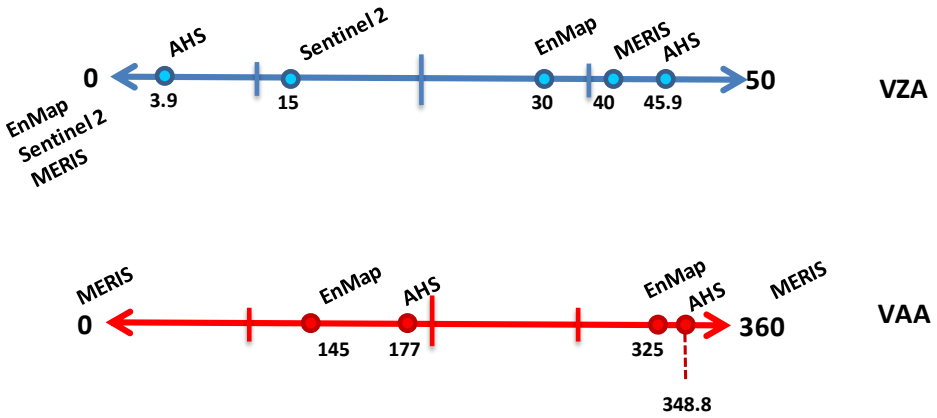

Figure 8. The Selected Sensors to be Simulated and their Viewing Geometry

Table 2. Various Sensors and their Spectral Range and Resolution

Sensor	Type	Range		Sampling Interval (nm)	No. of Bands	Spatial Resolution
AHS	Hyperspectral, Airborne	VNIR SWIR TIR	0.43 – 1.03 µm 1.55 – 1.75 µm 1.99 – 2.54 µm 3.3 – 5.4 µm 8.20 µm - 12.7 µm	30 200 13 300 400	20 1 42 7 10	2.5 to 10 m
EnMap	Hyperspectral, Satellite	VNIR SWIR	420 – 1000 nm 900 – 2450 nm	6.5 10	89 155	30 m
MERIS	Multispectral, Satellite	VNIR	390 – 1040 nm	2.5 – 30		260 x 300 m
Sentinel-2	Multispectral, Satellite	VNIR SWIR	490 nm, 560 nm, 665 nm, 842 nm 705 nm, 740 nm, 783 nm, 865 nm, 443 nm, 945 nm, 1375 nm 1610 nm, 2190 nm	65, 35 30 15 20 20 30 90, 180	4 6 3	10 m 20 m 60 m

As a second step, the possible illumination conditions of the study area were simulated. This involved a laborious task of calculating instantaneous solar azimuth and solar zenith angles for different times of the day and for different seasons, for a particular geographic location (see Appendix B). In the solar calculations, instantaneous solar azimuth and zenith angles, solar altitude, solar declination, day length, and extraterrestrial solar radiation were computed, among others. As a priority, the illumination conditions for Schiermonnikoog in June 19, 2005 at 11:10 AM, 11:29 AM, and 11:48 AM, which represent the date and time of acquisition of the AHS image strips, were computed (see Table).

Table 3. Illumination conditions of Schiermonnikoog during the date and time of AHS image acquisition

	Solar zenith angle [°]	Solar azimuth angle [°]	Solar altitude [°]	Solar declination [°]	Solar time [hs]	Extraterrestrial solar radiation [W/m2]	Day length [hs]
Output							
1. Schier 53.4 N, 6.38 E, 11:10 AM	**39.452**	**54.059**	**50.548**	**23.424**	**9.727**	**1021**	**16.7583**
2. Schier 53.4 N, 6.38 E, 11:29 AM	**37.250**	**47.993**	**52.750**	**23.424**	**10.043**	**1053**	**16.7583**
3. Schier 53.4 N, 6.38 E, 11:48 AM	**35.257**	**41.435**	**54.743**	**23.424**	**10.360**	**1080**	**16.7583**

Since the selected times were just a few minutes apart, the SZA and SAA did not vary differently. However, a different time of the same day will give a larger difference. These differences illustrate just how variant illumination angles could be over time thus, a need to have proper knowledge in solar radiation as well as in the study area is essential before acquiring satellite/airborne images from data providers, or before conducting flight campaigns. For the laboratory simulations, the illumination scenarios were chosen based on whether:

(1) The discrimination of key benthic cover types using optical remote sensing was achievable or not. For instance, the solar conditions during winter months such as January may be high, but the solar declination is negative, which means that the sun is located at latitudes below the equator (e.g., Tropic of Capricorn). For the case of Schiermonnikoog, this means low solar radiation due to the sun being far from the study area's location (at latitude 53^{o})

(2) The scenario reflects the operational setting of mussel bed monitoring requirements from a policy and management perspective.
To illustrate, fishing of mussels and cockles is only permitted on a certain date based on mussel inventory showing that there is sufficient quantity. Any remote sensing campaign should be done shortly before this date of decision making.

Therefore, the number of possible scenarios was reduced to remove undesired combinations. On the other hand, the varying viewing geometries of the sensors were integrated in the combinations as much as possible. It should be noted that the viewing azimuth angle of sensors could not be included in the simulations (see Discussion).

After many trial and error in the developing the optimal number of combinations, the final combinations are summarized in Table 4. One can see that a relative solar azimuth angle (SAA) is paired for each solar zenith angle (SZA), and simultaneously paired with 4 combinations of viewing zenith angles for airborne sensors (VZAA) and 3 combinations of viewing zenith angles for satellite sensors (VZAS). These are then tested for each of 6 benthic cover types, to give a total of 42 measurements for one single combination (7 per benthic cover type), for a grand total of 168 single measurements. With these pairs of combinations, the possible ranges in viewing geometry of the sensors (e.g., 0^{o} and 45^{o} represent min-max values of the AHS) as well as the best time and season for illumination conditions (e.g., SZA during the spring to summer months is 30-60^{o}) are sufficiently represented.

Table 4. Combination of Observation Geometries

	SZA	SAA	VZAA (Airborne)	VZAS (Satellite)	Benthic Cover Types (n = 6)	Total
1.	40	50	0, 15, 30, 45	15, 30, 45	Mussel, Oyster, Cockle, Mussel_B (with barnacle), Oyster B (with barnacle), Seaweed	42
2.	50	30	0, 15, 30, 45	15, 30, 45		42
3.	40	30	0, 15, 30, 45	15, 30, 45		42
4.	60	60	0, 15, 30, 45	15, 30, 45		42
					TOTAL:	168

3.4.2. Instrument Set-Up

The main instrument used for the simulation of varying observation geometries was a custom-made goniometer, a specialized device that measures bidirectional reflectance (see Coburn and Peddle (2006) for detailed information). Goniometers allow the manipulation of the sensor's viewing zenith and azimuth angles as well as manipulation of illumination angle (see Figure 9).

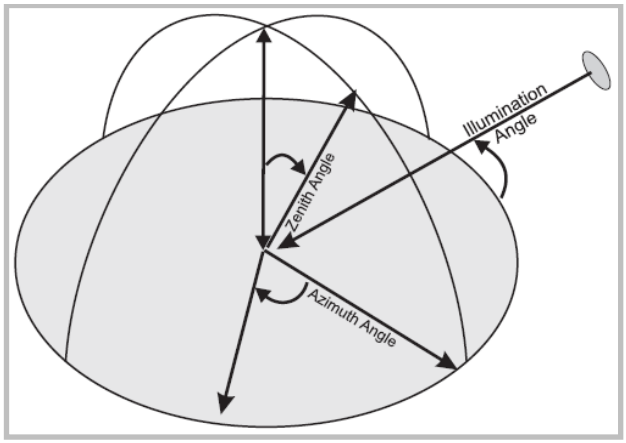

Figure 9. Mechanism of the goniometer
Source: (Coburn & Peddle, 2006, p. 246)

Mounted on the goniometer were the ASD pistol grip (to measure reflectance) and the tungsten filament lamp (to simulate solar radiation) (see Figure 10). A white Spectralon panel was used as white reference and basis for conversion from radiance to percent reflectance. The 1° field of view was used to allow the ASD to measure reflectance at a smaller surface area. In this way, scattering and atmospheric influences are minimized. The calculation of surface area was implemented using the formula provided in ASD Inc. (2008a). At a distance of 20 cm from the surface, the calculated diameter field of view is 22 cm.

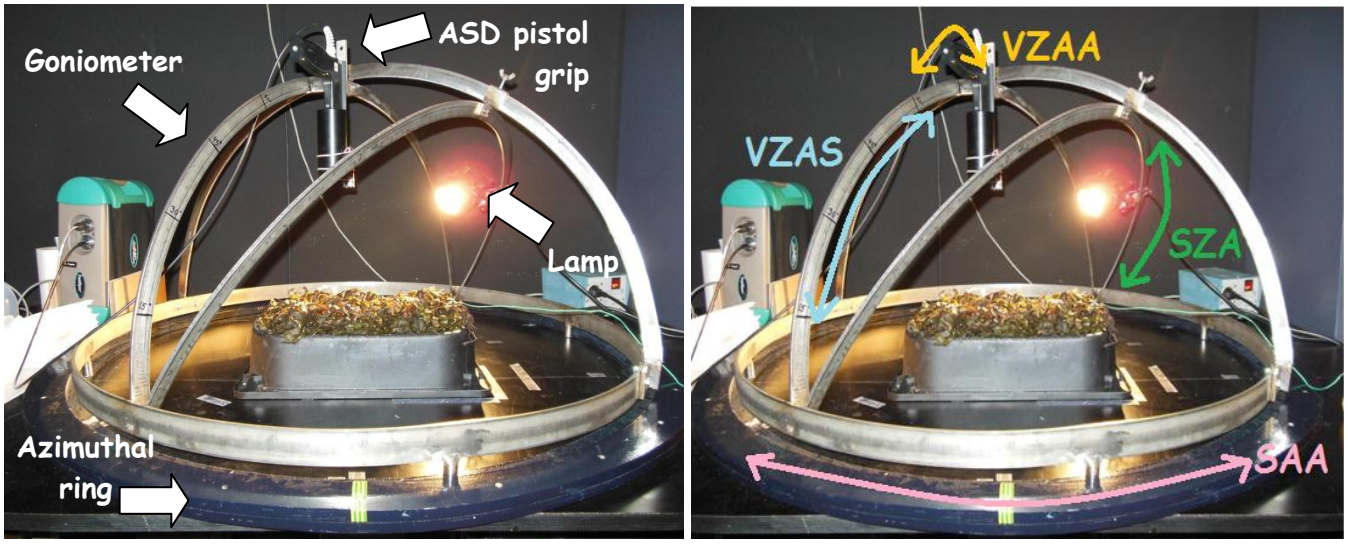

Figure 10. Goniometer Setup and Mechanism

To simulate the various combinations of observation geometry, the mechanism of the custom-made goniometer was defined by the author (see above Figure). First, the benthic cover type was placed on top of a black upturned Tupperware. This was done mainly for sanitary purposes of the experimental table and of the laboratory as a whole. The benthic cover type was spread evenly across the surface of the Tupperware to maximize its surface area. Note that the dimensions of the Tupperware were 41 x 29.5 x 10 cm, while earlier, the calculated diameter captured by the 1^{o} FOV was 22 cm. The differences in surface area will be discussed further in detail in Section 4.1.3. The position of the Tupperware on the table was marked for uniformity in the succeeding measurements. The ASD was mounted on the goniometer, assuming a zenith angle of 0^{o} when directly overhead the central part of table and of the Tupperware. The goniometer has three rings, one of which is stationary. This is called the zenith arch and is represented by the ring marked VZAA. The other two rings, represented by VZAS and SZA, are attached to the zenith arch and are moved using the adjustable valves. One ring supports the ASD while the other supports the lamp. All three rings are supported by the azimuthal ring, which has a diameter of 102 cm. The three rings were marked with 15^{o} increments for the simulation of the various angles. The ring supporting the lamp source was titled 30^{o} from zenith to account for the size of the lamp. The goniometer is placed on top of a wooden ring that had a slightly bigger diameter than the azimuthal ring to allow sufficient space for the movement of the entire goniometer within the said ring. This ring was also marked with 15^{o} increments to model different SAAs. The respective ring and direction to model VZAA, VZAS, and SZA are illustrated in Figure 10.

3.4.3. Spectral Measurements of Simulations

The spectral measurements of the benthic cover using the different combinations of observation geometry were executed, following the order in Table 4. First, the benthic cover samples were rinsed with seawater to remove sand. Thus, in the first few minutes of measurements, the samples were relatively wet, but in succeeding measurements, exposure to high energy coming from the lamp quickly dried out the samples. One measurement was recorded for each combination (e.g., SZA-SAA 40^{o}, 50^{o}, VZAA_0^{o} = 1 measurement). Spectral recordings were done through the ViewSpec Pro while additional notes as well as photos were taken (see Appendix A). The calibration of white reference using the Spectralon panel was done every 10 minutes. The recorded spectra, which were in radiance values, were then splice-corrected and converted to reflectance values.

3.5. Image Pre-Processing

3.5.1. Hyperspectral Datasets

The hyperspectral imagery used in this study was produced by the Airborne Hyperspectral System (AHS), an airborne hyperspectral line-scanner radiometer operated by the Insituto Nacional de Tecnica Aeroespacial (INTA). The AHS has a 90^{o} field of view and records radiance in 80 bands ranging from 0.43-12.7 μm. The spectral bandwidths of the 80 bands covering the Visible-Near Infrared (NIR) to the Thermal Infrared parts of the electromagnetic spectrum are found in Table 5. AHS images can have a spatial resolution of 2.5 to 10 m and a 12 bit radiometric resolution.

Table 5. Spectral Bandwidth of AHS Imagery

Optical Port	Number of Bands / Numbering	Spectral Region	Bandwidth
1 – Visible to Near Infrared	20; Bands 1-20	0.43 – 1.03 μm	30 nm
2A – Shortwave Infrared	1; Band 21	1.55 – 1.75 μm	200 nm
2 – Shortwave Infrared	42; Bands 22-63	1.99 – 2.54 μm	13 nm
3 – Mid Infrared (TIR)	7; Bands 64-70	3.3 – 5.4 μm	300 nm
4 – Long Wave Infrared (TIR)	10; Bands 71-80	8.20 – 12.7 μm	400 nm

Source: Adapted from Reusen (2005, p. 17)

The Vlaamse Instelling voor Technologisch Onderzoek (VITO), in cooperation with INTA, conducted a series of AHS flight campaigns in 2005, one of which was over the adjacent islands of Ameland and Schiermonnikoog. On June 19, it recorded three image swaths (each of which was later cut into two parts for each island) on a flight path that followed the orientation of the islands' shapes (elongated from west to east).

The strips were flown with the following time intervals: 11:10 am, 11:29 am, and 11:48 am (local time). These were then reprocessed by VITO into level 2 product images, which were then made available together with corresponding hierarchical data format (HDF) files (free standing metadata files) (see Table 6).

Although another hyperspectral dataset (HyMap) was available for this study, the AHS imagery was selected because it had more leverage in being validated in terms of the output classification. Validation data, in the form of GIS shapefiles of mussel beds were more available in 2005 when the AHS images were acquired, than for HyMap, which was in 1999 (see Section 5.2.5). It should be noted that initially, it was only Schiermonnikoog that was chosen for the study, but through further investigation of VITO's flight campaigns in 2005, it was discovered that Ameland was flown together with the aforementioned island. Moreover, shapefiles of mussel beds in Ameland were also available for 2005 thus, allowing for more leverage in validation.

Table 6. AHS Imagery Acquired from VITO

Name	Description	Latitude (WGS_1984)	Longitude (WGS_1984)	Pixel size
(1) 050619_WADAM_01	Ameland 1st strip	5° 29' 40.01"	53° 29' 38.57"	0.000042 Degrees
(2) 050619_WADAM_02	Ameland 2nd strip	5° 31' 5.39"	53° 28' 44.74"	0.000042 Degrees
(3) 050619_WADAM_03	Ameland 3rd strip	5° 30' 39.93"	53° 27' 49.96"	0.000042 Degrees
(4) 050619_WADAM_01	Schiermonnikoog 1st strip	5° 58' 50.50"	53° 31' 7.58"	0.000043 Degrees
(5) 050619_WADAM_02	Schiermonnikoog 2nd strip	5° 59' 16.90"	53° 30' 24.09"	0.000043 Degrees
(6) 050619_WADAM_03	Schiermonnikoog 3rd strip	5° 59' 9.52"	53° 29' 29"	0.000043 Degrees

VITO processed the flight strips over Ameland and Schiermonnikoog using Product Level 2 of the Central Data Processing Center (CDPC), a custom-made hardware and software system designed to "(a) simulate operations and (b) to enhance the development of algorithmic image processing components within an operational context" (Biesemans et al., 2007, p. 2). Level 2 image processing means that the images have underwent standard system corrections and radiometric calibration and are additionally processed for geometric (and geocoding) and atmospheric corrections. Geometric corrections were done through direct georeferencing (DG), the "direct measurement of the position (by means of a GPS) and orientation parameters (by means of an IMU) of a sensor" (Biesemans et al., 2007, p. 8). For the atmospheric corrections, the MODTRAN 4 radiative transfer code model was applied. This code calculates the surface radiance of each pixel in an image based on information from at-sensor radiance, solar radiation, and atmospheric influence on radiance. In principle, MODTRAN4 settings should be configured according to the pixel orientation relative to sun and sensor position as well as to in-situ spectral measurements. In doing so, atmospheric parameters such as visibility, water vapor content, and aerosol type, are "altered to better describe the atmosphere…until the calculated target reflectance is in good accordance with the measured reflectance" (Biesemans et al., 2007, p. 9). However, pixel-by-pixel atmospheric correction is impractical in terms of computing time. Hence, the CDPC used pre-calculated look up tables (LUT) of radiative transfer codes that are generated from interpolating from a set of samples in a given geometry space for each image and for each spectral band. The result is a MODTRAN4 configuration that is "on the fly", one whose parameters can be modified with available and site-specific in-situ measurements (Biesemans et al., 2007).

3.5.2. Assessment of Image Quality

A. System and Radiometric Corrections

In the evaluation of the pre-processed dataset, it was observed that the spectra of pixels from band 22 until band 63 (2-2.5 μm) had poor signal to noise ratio (SNR). The spectra of pixels in this region appeared to be spiky, if not having 0 values. Such observation was also noted by other authors (Banskota, 2006; Mulatu, 2006) and indicated what VITO reported as a linear degradation of sensor optics during the flight day caused by ice and dirt accumulation. As a result, image reflectance in this range poorly corresponded to actual surface reflectance. VITO was able to recalibrate and reprocess the dataset accordingly, but the undesired values remained. Also, in their recalibration, the spectral range of the images was slightly different from the original/published range. In particular, the starting band was shifted from 0.43 μm to 0.455 μm and the end band from 12.7 μm to 12.89 μm.

Further explanation was sought and was found in a status report on the AHS sensor by INTA, the operators of the AHS. Contrary to the earlier explanation by VITO, sensor degradation was actually caused by "dust deposition and salt action on the rotating mirror and telescope surfaces" (Gomez et al., 2007, p. 2). Apparently, the system design for the Port 2 channel (SWIR) of the AHS sensor was such that it produced a considerable amount of noise thus, low SNR. Such already low SNR values were only aggravated further during the flight campaigns in 2005 to a level that was "not acceptable for scientific applications" (Gomez et al., 2007, p. 2). The report then further discussed about a system upgrade in the beginning of 2007, which included a replacement of the Port 2 diffraction grating from 12 μm (original) to 18 μm, ultimately affecting the spectral bandwidths of bands 22-63 of the AHS (Gomez et al., 2007). In conclusion, this important account from INTA provides sufficient reason to exclude the bands in the SWIR region from the analysis.

B. Geometric Corrections

The AHS images, which were originally projected in WGS 1984 (geographic coordinate system), were reprojected into the Dutch RD (projected coordinated system) (Table 7). This was done not only to take advantage of the coordinated system dedicated to the country, but also to match with the coordinate system of the mussel bed shapefiles. In doing so, a proper overlay of the shapefiles on the images is ensured. However, the reprojection was not as straightforward as expected. The steps taken in completing the reprojection are discussed next.

The reprojection was implemented using the Convert Map Projection functionality in ENVI (RD_New projection; Triangulation method; Nearest Neighbor resampling). The initial run revealed that the RD_New projection in ENVI did not produce the actual Dutch RD, despite editing this projection's metadata according to the Dutch RD coordinate system parameters (e.g., datum, false easting and northing). This was tested by overlaying vector shapefiles (in Dutch RD) of urban structures in the two islands onto the reprojected image, and seeing a large offset of the latter from the former. Reprojection using other software programs like ArcGIS and ERDAS were considered but were not done as these programs crashed due to the large amount of data processing required for the AHS images. To resolve this, an image to image registration in ENVI was then explored. First, the wrongly reprojected image was saved as a geoTIFF file, an image file of smaller file size. This geoTIFF file was then opened in ArcGIS and was successfully reprojected into Dutch RD. Afterwards, an image to image registration was performed between the wrongly reprojected image (RD_New) and the geoTiFF file (Dutch RD). Five tie points with an RMSE of less than 0.1 was achieved for each image pair. Finally, the results of the image registration were successful, as the offset between vector shapefiles and the newly reprojected images was reduced to 1-3 pixels (3-9 meters). However, the process of image to image registration took a lot of processing time and the output images greatly increased in disk space (up to 9 gigabytes per image). Foreseeing that the amount of data to be processed would affect subsequent image processing steps, other alternatives were sought. At this stage, the Match Existing File option in the Convert Map Projection ENVI functionality was found. This option allowed for one image to adapt the exact projection parameters of another. To proceed, the original image was first saved as a geoTIFF file, which was then reprojected into Dutch RD through ArcGIS. The reprojected geoTIFF file then served as the file whose projection was to be matched.

Table 7. Reprojected AHS Images

Name	Description	Latitude (Dutch RD)	Longitude (Dutch RD)	Pixel size
(1) 050619_WADAM_01	Ameland 1st strip	162117.5066	612152.6173	3.681463 Meters
(2) 050619_WADAM_02	Ameland 2nd strip	163694.8184	610492.5031	3.617951 Meters
(3) 050619_WADAM_03	Ameland 3rd strip	163228.1362	608797.9761	3.70175 Meters
(4) 050619_WADAM_01	Schiermonnikoog 1st strip	194367.4342	615228.1508	3.766698 Meters
(5) 050619_WADAM_02	Schiermonnikoog 2nd strip	194865.0569	613938.1440	3.810827 Meters
(6) 050619_WADAM_03	Schiermonnikoog 3rd strip	194743.4053	612239.5238	3.858336 Meters

C. Atmospheric Corrections

1. Inconsistencies in MODTRAN4 Settings

As previously mentioned, the image swaths of both Schiermonnikoog and Ameland were chosen as viable candidates for image classification. In particular, the swaths that had the most coverage of the mussel

beds in the tidal mudflats south of the island were used. For Ameland, this was the third swath, and for Schiermonnikoog, the second and third swaths. Upon examination of the HDF files, it was found that the MODTRAN settings applied were different between the two islands (see Table 8). For example, the visibility parameter for Schiermonnikoog was pegged at 60 km while for Ameland was 25 km. These values were most likely operator-defined, as the default value in the MODTRAN4 settings is 23 km (Biesemans et al., 2007). The values do not seem to be attuned with each other and one must question if such a difference in visibility can take place during the time span of flying between the two adjacent islands on a sunny day at spring time. Moreover, a quick check of the water levels (in cm) of the islands revealed that it was low tide during noontime of June 19, 2005 (see *Historische waterkwaliteitgegevens* from Rijkwaterstaat website). To solve this problem, VITO was contacted and requested to re-process the imageries to have the same settings.

Table 8. MODTRAN4 Settings Applied to Ameland and Schiermonnikoog

Parameter	Abbreviation	Schiermonnikoog Original Settings	Ameland Original Settings	Final Settings
MODTRAN4CardConfiguration (http://www.vito.be)	NA	End pathname: /uav.archiver	End pathname: /CDPC	End pathname: /CDPC
Vertical Water Vapor Column	H2OSTR	1.73 gm /cm^2	1.5 gm /cm^2	1.72 gm /cm^2
Aerosol Optical Properties	H2OAER	T*	T	T
IHaze	IHaze	1	1	1
Visibility	Vis	60 km	25 km	60 km
*modified to reflect the changes from the original relative humidity profile arising from the scaling of the water column				

2. Anomalies in Reflectance Values

Another problem encountered during assessment of atmospheric corrections was the discrepancy between reflectance values of overlapping areas of adjacent flight strips. Reflectance values were quite different between the second and third strips of Schiermonnikoog, despite the lapse of only 20 minutes observation time between. Again, this inconsistency may be caused by the degradation of sensor optics. To alleviate this problem, the method of Verbeke et al. (2006) was adapted. Verbeke et al. (2006), in their pre-processing of the same Schiermonnikoog AHS dataset, implemented in ENVI-IDL a band matching algorithm that tried to match the reflectance of overlapping regions of two strips, assuming that these were flown simultaneously. The algorithm employed a multiple linear regression technique that normalizes the reflectance of two images. Essentially, the R values are re-expressed to match one strip to another and the coefficient of regression line (R^2) is used as a predictor. The R^2 should have values of 0.8 or higher in order to retain good bands. This band matching algorithm was considered a more robust method compared to Cross Track Illumination, Histogram Matching, and Color Balancing functionalities in the ENVI software. The developed algorithm is summarized as:

$$target_{DN} = f(x,y, original^{DN}), \text{ with } f \sim \text{linear or quadratic function}$$

where: both x and y were found to contribute statistically significantly to the regression analysis

Source: (Verbeke et al., 2006, p. 8)

5.2.3. Other Data

GIS shapefiles of mussel beds surveyed in June-July 2005 were generously provided by the Institute for Marine Resources and Ecosystem Studies (IMARES), the research institute primarily involved in the monitoring of mussel beds in the Dutch Wadden Sea (TMAP, 2011). In their annual field surveys, IMARES maps the location and area (border/contour) of stable mussel beds (Fey et al., 2011). For some individual beds, they go beyond these basic measurements and record other data such as coverage (percentage of live mussels in a bed) and size and biomass of mussels as well as other benthic cover present in the bed (Fey et al., 2011). These beds include Beds 502 and 503, which are located in the tidal mudflats south of Ameland, and Beds 603, 606 and 607 for Schiermonnikoog. A total of 102 mussel bed shapefiles were provided by IMARES. Of these, only 85 were within the coverage of the AHS image swaths, 7 of which with only partial overlap (see Figure 11). Other beds, including Bed 603, were excluded from further analysis.

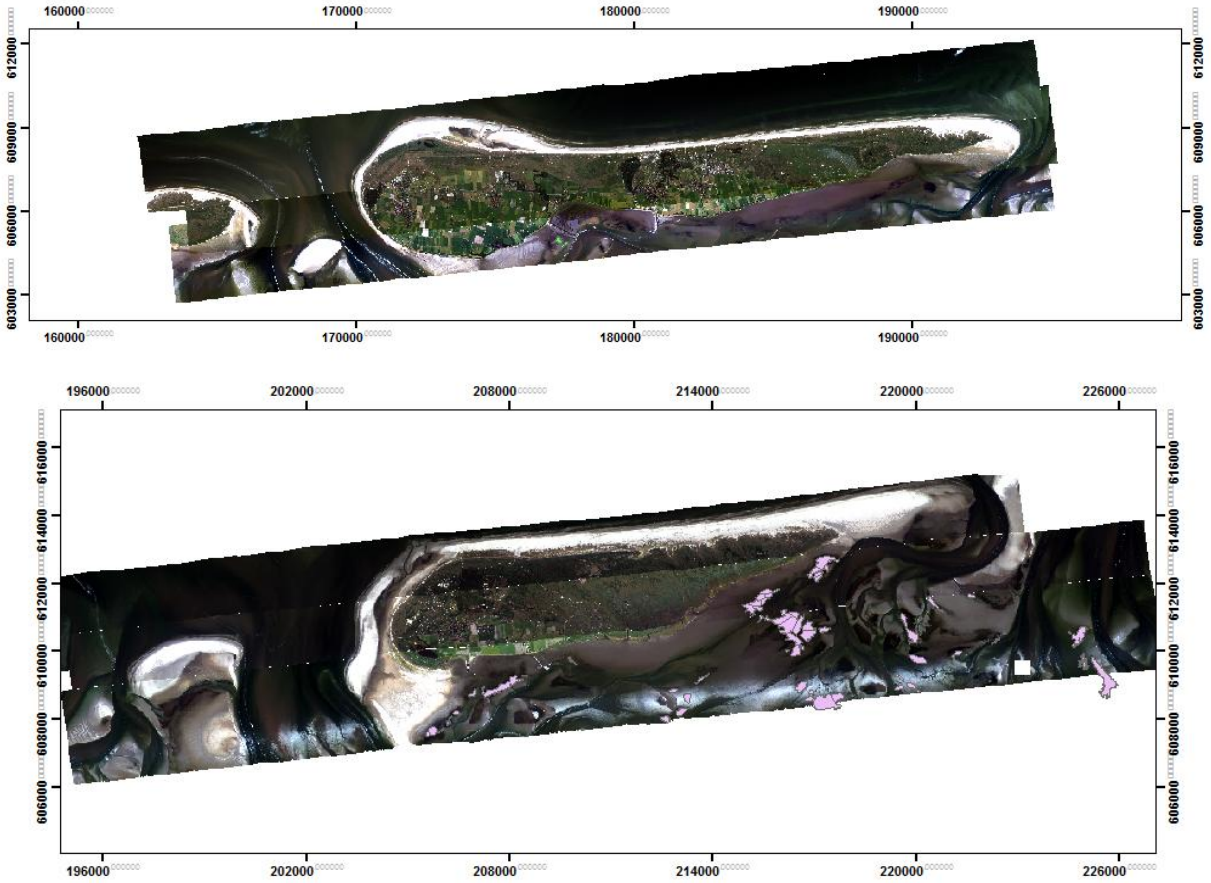

Figure 11. Location and coverage of mussel bed shapefiles within the AHS imagery of Ameland (upper map) and Schiermonnikoog (lower map).

4. Results and Discussion

4.1. Investigating the Spectral Distinctness of Blue Mussels & Japanese Oysters

4.1.1. Visual Differences

A. Reflectance Curves of 8 Benthic Cover Types

The mean spectral reflectance of the original 8 benthic cover types measured in laboratory conditions are found in Figure 12. For clarity, an offset was applied to emphasize the different spectra. Overall, the general shape of seaweed (a type of vegetation) and shellfish spectra are very similar. These are especially apparent in the absorption depths at around 1400 nm and 1900 nm caused by water molecules. An absorption (of varying depths) can also be observed in the 680 nm region in all the benthic cover spectra except for the razor shell, which continues to increase up to 750 nm. These absorption features can be better visualized when the spectra are continuum removed (see Figure 13). With the continuum removed spectra, the depth of the absorption of seaweed spectra at 680 nm is deeper than the shellfish spectra. This can be attributed to chlorophyll content present in vegetation species. Moreover, minor water absorption bands at 980 nm and 1200 nm are seen more clearly. Meanwhile, the shellfish spectra exhibit one or two small absorption features in the 2300-2480 nm region. This feature is characteristic of materials containing carbonates, as such is the case of shells.

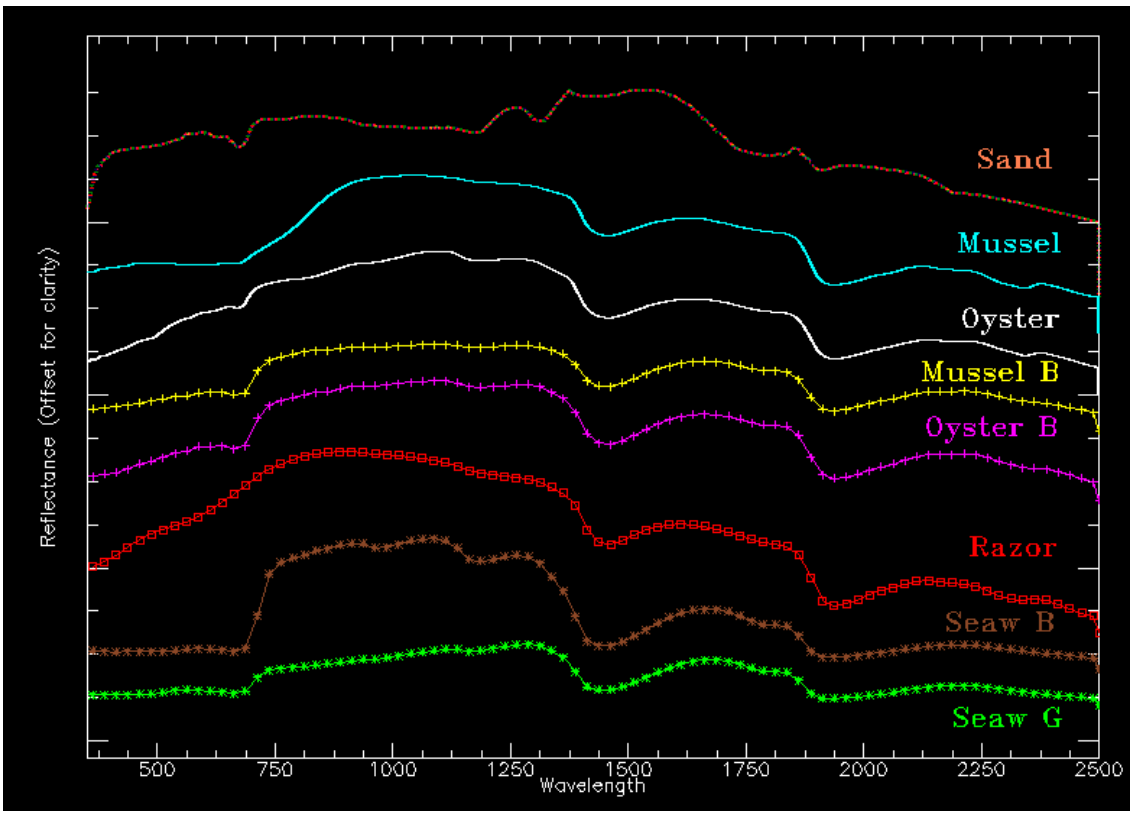

Figure 12. Mean reflectance curves of 8 benthic cover types + sand

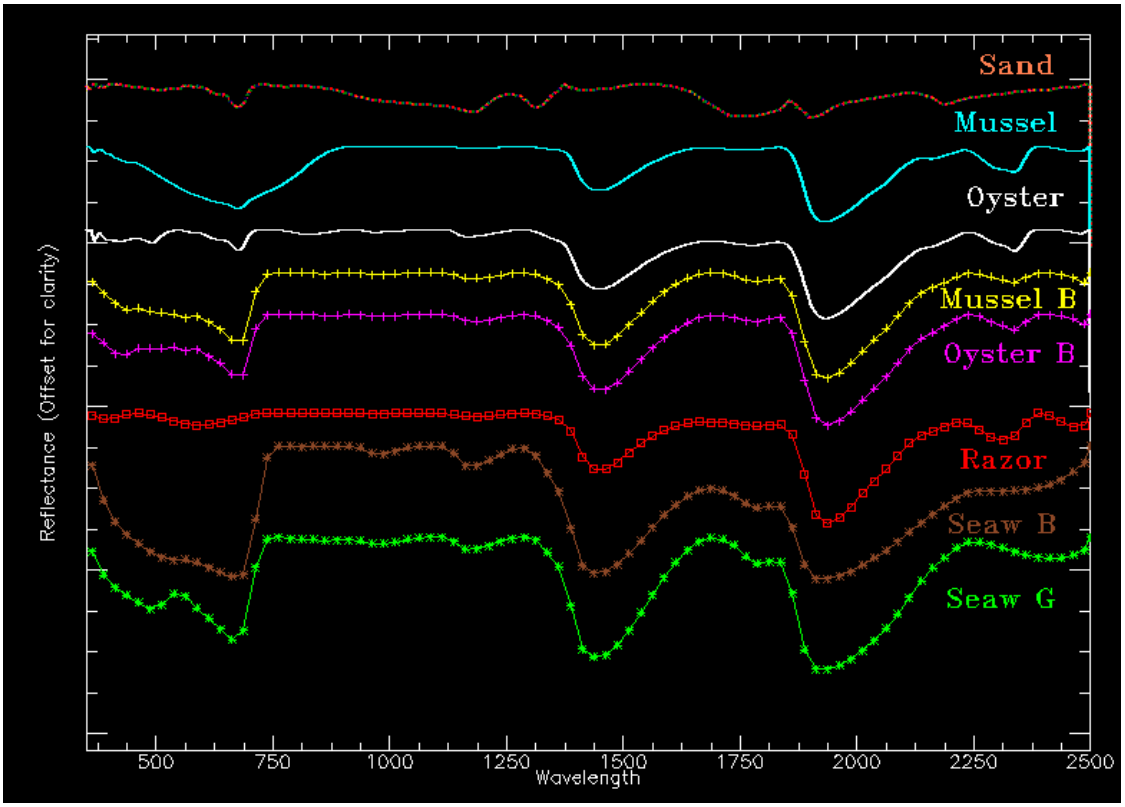

Figure 13. Mean reflectance curves of 8 benthic cover types + sand, continuum removed.

B. Comparison between Blue Mussel & Pacific Oyster Reflectance Spectra

The similarities and differences in the blue mussel and Pacific oyster shell spectra are visualized in Figure 14. The left-side plot shows the average reflectance of the two shellfish species vis-à-vis the spectra of calcite in the VNIR-SWIR range. Certain absorption features are evident and are emphasized in the right-side plot featuring the continuum removed version of the same spectra. As mentioned earlier, water absorption bands are observable at around 1200 nm, 1400 nm and 1900 nm. An absorption depth is also visible at 2300 nm and at 2500 nm at a shallower depth, both of which are characteristic of carbonate spectra. The plots show that both mussel and oyster spectra exhibit some similarities with the calcite spectra, as both are composed of varying degrees of calcium carbonate. There are, however, other absorption features that are unlike the calcite spectra, such as the absorption depths at around 680 nm as well as 500 nm in the case of the oyster spectra. A noticeable difference between the two species can also be depicted in the 350 to 600 nm range. The reflectance values of the oyster exhibit a gradual increase towards 600 nm while the mussel reflectance resembles a flatter pattern. These differences are possible distinctive features, which will be investigated further through the statistical tests.

Furthermore, the mussel spectrum is seen to have slightly higher reflectance values than the oyster spectrum and is contrary to what the colors of their shells suggest. It may be due to the fact that the mussel shell, although naturally blue, is subject to a form of “intertidal weathering.” The ebb and flow of the tide plus the clustering with other shellfish cause the blue color to fade to a whitish gradient, thus also affecting the reflectance of the shell.

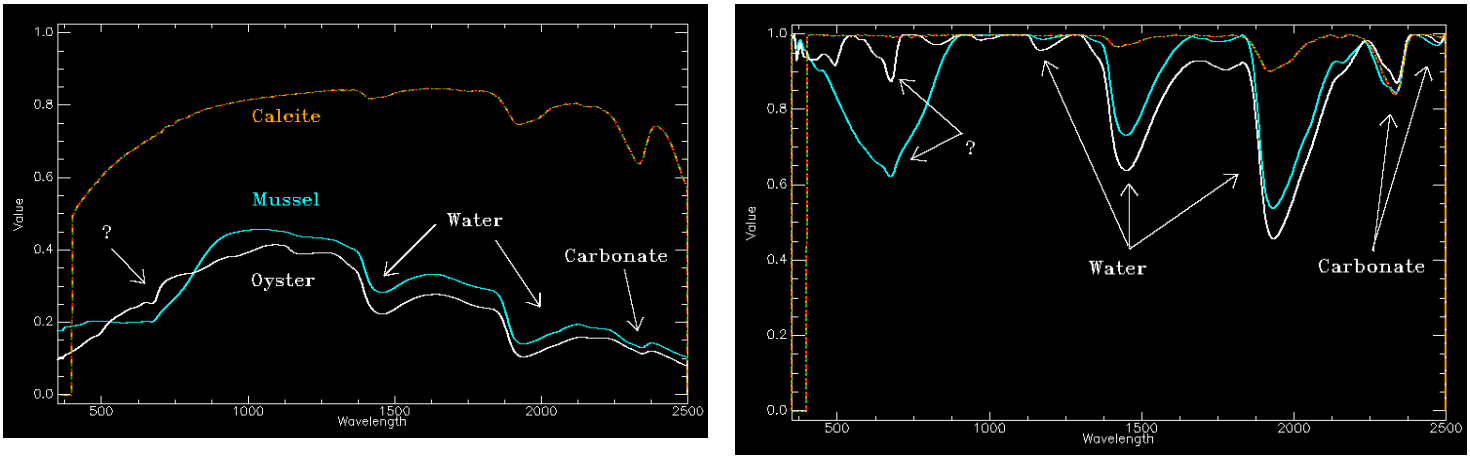

Figure 14. Blue mussel and Pacific oyster spectra plotted with calcite (left). Continuum removed spectra (right).

4.1.2. Statistical Differences

A. Results of Mann-Whitney U Test

Recall that the Mann-Whitney U tested for the statistical difference between the median reflectance of two samples per measured wavelength. The results show that out of the 15 benthic cover pairs, a minimum of 7 pairs and a maximum of 13 pairs were found to be statistically different ($p < 0.05$) at a certain given wavelength (see Figure 15). For example, in the 700 nm region, the lowest frequency (7 pairs) of significant pairs can be found. This means that benthic cover species are hard to be discriminated from each other using this particular region of their reflectance spectra. Meanwhile, the highest frequency of significance of 13 pairs can be differentiated in 67 wavelengths. These wavelengths are all found within the visible range between 353 nm and 523 nm and a single band in the red region at 701 nm. This means that the visible range holds the most potential for discriminating between the 6 benthic cover types, and should be the region of main interest when examining the image endmembers of the AHS. However, the spectral range of the provided images starts at 0.455 µm (455 nm; see Section 3.5.2.A.). This reduces the number of potential wavelengths to 28 (455 nm, 498-523, and 701 nm). It must also be noted that of the 13 pairs, no pairing was found to be significantly different at 0.01, which is the more robust level of significance. At the frequency of 12 pairs, however, there are 77 wavelengths significant at 0.01, 74 of which coincide with the AHS spectral range. These are found between 600 to 700 nm or between the yellow to red part of the visible spectrum. These wavelength are then also included in the comparison with the AHS images.

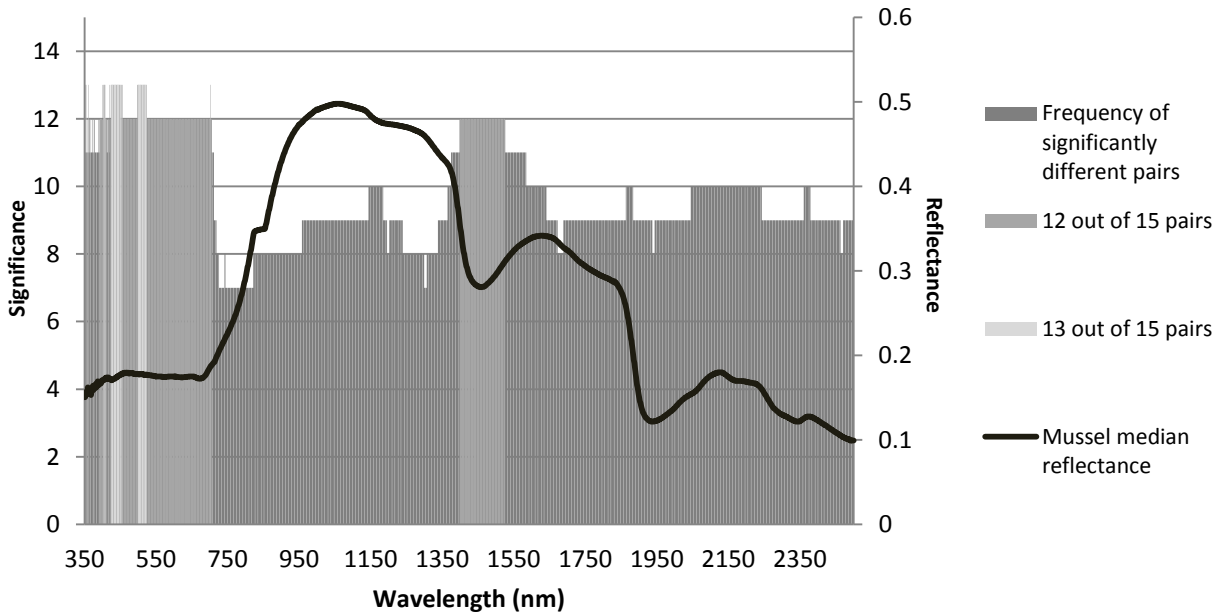

Figure 15. Frequency of significantly different pairs

The difference between the median reflectances of the mussel and oyster spectra is also analyzed separately. The Mann-Whitney U revealed that the two species can be differentiated in 78 wavelengths (350-427 nm) at a 0.01 level of significance and an additional 28 wavelengths (428-455 nm) at a 0.05 level of significance for a total of 106 significant wavelengths. This means that the mussel and oyster spectra can be discriminated the most using the visible range, particularly within 350-455 nm. The test partly confirms the visual comparisons, wherein a difference in the 350-600 nm range was indeed observable. However, the absorption features observed visually and with the continuum removal (e.g., 2300 nm) were not found to be statistically different between the two spectra. Hence, if only the statistically significant bands were used for analysis with the AHS spectral range, this would be limited to the violet part of the visible range. This is undesirable mainly because of the noise that is more prevalent in this part of the region due to scattering of the shorter wavelengths. Moreover, the spectral range of the provided AHS images begins at 455 nm, which leaves only one out of the 106 potential wavelengths for comparison.

4.1.3. Discussion

The spectral reflectance of the blue mussel and Japanese oyster in the VNIR-SWIR region were investigated and were found to be unique from each other. However, the general shape of their spectra was very similar except for the 350-600 nm range. This was further confirmed through the Mann-Whitney U test, which showed significant difference only between 350-455 nm. Absorption features were not very distinctive in the normal reflectance curves but were more evident using continuum removal. The continuum removed spectra showed that both mussel and oyster spectra had absorption features at 2300 nm and 2480 nm, which are characteristic for carbonates, particularly calcite (Clark, 1999). Absorption features at 1400 nm and 1900 nm were attributed to water, although calcite also has a strong absorption at 1900 nm. This is because "reflectance spectra are extremely sensitive to the presence of water" and is "nearly ubiquitous in carbonate minerals" (Gaffey, 1986, p. 156). Other absorption features were also found, but were not attributed to carbonate or to any other chemical that may compose the mussel and oyster shells. It may be noteworthy to state that the absorption feature at around 680 nm is quite reminiscent of chlorophyll, a chemical characteristic of vegetation species. However, a lack of studies on the reflectance spectra of the outer layer of shells (not to be confused with studies pertaining to the nacreous/pearly inner layer of shells) cannot confirm this. One must then remember that a shell's composition is "a biologically mediated combination of organic substances with inorganic material" (Jacob et al., 2008, p. 5402) whose biomineralization process is dependent on its environmental conditions (Farson, n.d.). Further investigation is then required in order to better understand the spectral features exhibited by these two species. Chemical analysis using X-ray Diffraction (XRD) and other spectroscopy methods are suggested.

Further statistical analysis was done to test the difference not only between the median reflectance of mussel and oyster spectra but also between other benthic species commonly found in the study area. The results of the Mann-Whitney U revealed that no single wavelength could discriminate between all 15 pairs. Of the possible 15, the highest frequency gained was 13 pairs. The species were found to be most differentiable in the visible range, particularly between 353 nm and 523 nm and 600 to 700 nm (for 12 significant pairs at a 0.01 level of significance). These results make sense since the general shape of the benthic cover is similar, but variations in their spectra can indeed be seen within the 350-500 nm region. Meanwhile, discrimination among the benthic cover types are also high around 600-700 nm or the red-edge region. This matches the findings of Kumar et al. (2010) wherein they tested for the spectral difference between 155 vegetation pairs and found that the red-edge region was one of the regions where most pairs could be discriminated. Despite that there was only one vegetation species included in the statistical test, the reflectance spectra of the shellfish species also showed absorption features around 680 nm, which ultimately contributed to the results of the statistical tests.

4.1.4. Propagated Errors

One must not overlook the consequences of experimental errors, as they may affect the results of the analysis. One of which is the lack of repeated (recorded) measurements per benthic cover species. Only five measurements per species were recorded using the contact probe. Thus, the variations in the spectra of the

mussel population, for example, could not be fully represented and the population could not be assumed to be normal (according to the Central Limit Theorem), hence, the appropriateness of the use of the Mann-Whitney U test for this case. As much as the said test solves the problem of limited number of samples per species, using sufficient number of samples (at least n=20) is still recommended. Furthermore, the mean reflectance spectra of the mussel and oyster may not be truly reflected by the 5 measurements, therefore the remark on the mussel reflectance spectra being higher in values than its oyster equivalent may not be valid.

4.2. Simulation of Varying Observation Geometries

4.2.1. Effect of Viewing Geometry to Reflectance Values

A total of 168 spectral measurements of the benthic cover samples per unique combination of observation geometries were modeled in laboratory conditions. An example of the results is found in Figure 16 for oyster spectra.

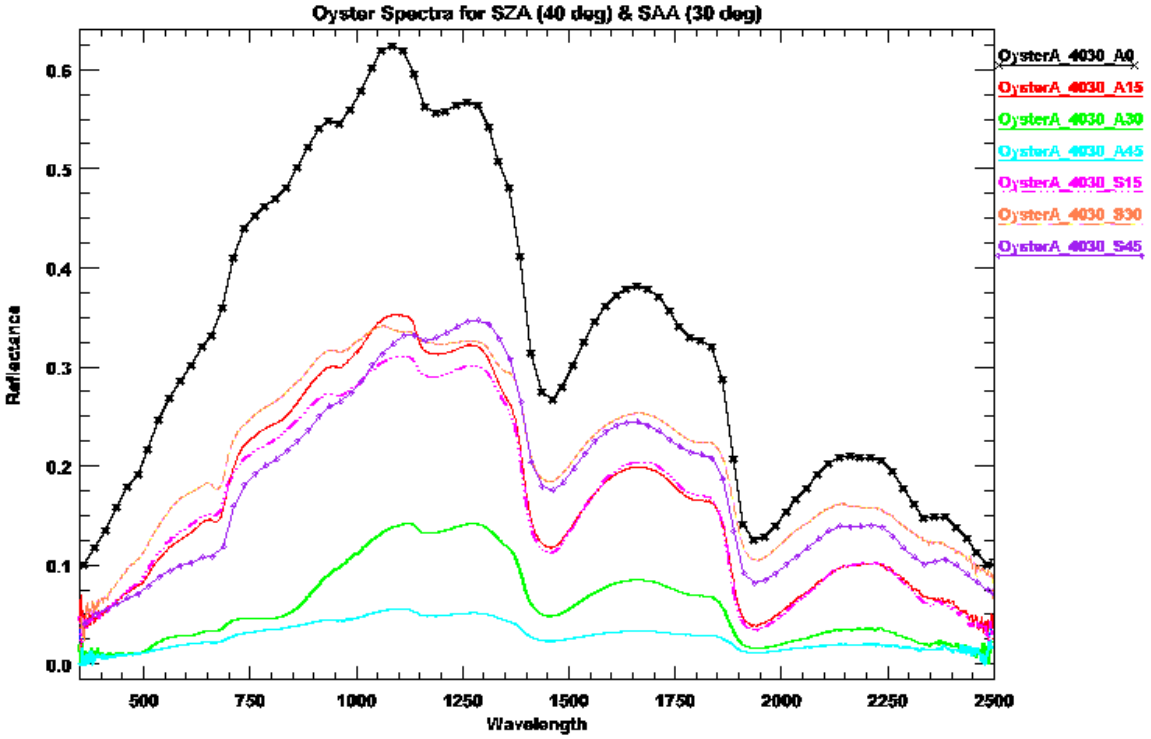

Figure 16. Oyster reflectance spectra in different observation geometries

From the reflectance of oyster at nadir (VZAA = 0°), the succeeding larger viewing angles have greatly decreased in reflectance values. For instance, the change from 4030_A0 to 4030_A15, or a 15 degree increase in viewing angle for airborne sensors, shows a 49% decrease in oyster mean reflectance. Consequently, as the sensor (ASD) moves father from the samples being measured, the ability of the sensor to detect the oyster spectra gets weaker, hence, resulting in lower reflectance values. In particular, the VZAA at 30° and 45° result in reflectance values smaller than 0.1 (green and blue spectra). On the other hand, the change in reflectance values of 4030_S15 from 4030_A0 (or alternatively, S0, since the nadir position of the ASD is the same for both airborne or satellite simulations) shows a decrease of 51%, which is comparable to the decreased signal obtained with airborne sensors. However, the succeeding measurements for VZAS do not show large differences as compared to those of VZAA. In fact, at 4030_S30, the reflectance of the oyster is slightly higher than at 4030_S15. These observations may be attributed to the difference in distance covered by the ASD when it is moved in 15° increments along the supporting arch compared to the same movements in the VZAS arch (refer to Figure 10).

The 42 spectral measurements taken for Cockle are plotted in Figure 17. Similar to the case of SZA40 and SAA30 combinations explained for the oyster spectra, the cockle spectra also shows the highest reflectance values in this particular combination. Differences, though, could be seen in the highest reflectance

plotted, which is not 4030_A0, as in the case of oyster spectra, but 4030_S30. A possible explanation for this is in the arrangement of the oysters on the surface of the Tupperware. Since the goal is also to partly mimic the assemblage of these benthic cover in their natural environment, some of the oysters were positioned upright while most were laid flat in irregular patterns (see Appendix A). For the cockles, the matter of either flat or upright positioning was of no importance because of their relatively small sizes.

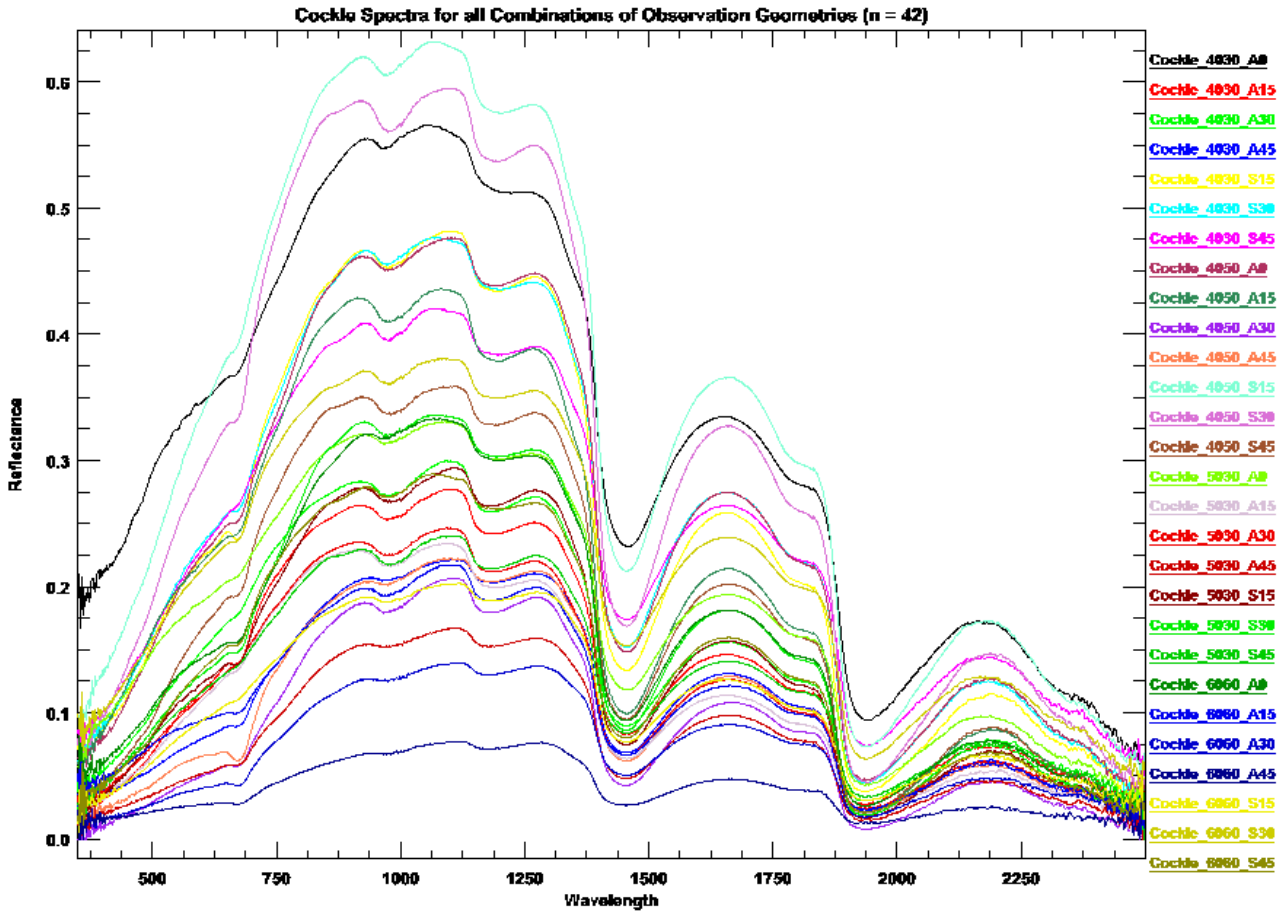

Figure 17. Cockle reflectance spectra for all combinations of observation geometries

The remaining plots for other benthic cover spectra are given in Appendix C. Without going into each description of the results of the spectral measurements in all 168 combinations, it is safe to assume that the benthic cover all exhibited maximum reflectance at SZA40 and SAA30, particularly for VZAA 0^{o}, 15^{o} and VZAS 15^{o}. The lowest reflectance values or the lowest signals were for SZA60 and SAA60, where the lamp was positioned at large angles, which facilitate scattering as well as shadowing. The scattering angle, or the "angle at the view point between vectors pointing toward the sun and the sensor" (TeraScan, 2002, para. 1) is largest when both solar viewing angle and sensor viewing angle are positioned almost at surface level with the sample being measured. In the combinations, the scattering angle is largest for reflectances recorded at 6060_A45 and 6060_S45.

4.2.2. Propagated Errors

The results of the simulation of varying observation geometries cannot be reported without acknowledging the errors that were made during the spectral measurements. These errors can be grouped into three: (1) condition of benthic cover samples; (2) mechanism of the goniometer; (3) human error.

A. Condition of Benthic Cover Samples

The simulation experiments started a week after returning from fieldwork. At this time, the purpose of the experiment was to determine the effect of various viewing and illumination conditions on the spectral reflectance of the collected benthic cover. With this in mind, various combinations of solar zenith angles (0,

15, 30, 45) and viewing zenith angles (0, 15) were. However, such combinations needed to be reevaluated. To simulate real in-situ conditions means considering the practical range of viewing and illumination variability, which is location-dependent. This means factoring in only the possible combinations of solar zenith angles (SZA) and viewing zenith angles (VZA) with respect to the geographic location of the study area. For example, in the aforementioned experiment, a solar zenith angle of 0 degrees was simulated in the study, where as in the latitudinal location of Schiermonnikoog (53^{o}N 6^{o}E), only solar zenith angles in the 30-88 deg range exist. Moreover, other factors of viewing geometry were failed to be considered, such as the relative solar azimuth angle (SAA) and the relative viewing azimuth angle (VAA). As a result, the said experiment needed to be redone, with the important parameters for selection kept in mind. However, due to the difficulties of selecting the final combinations of varying observation geometry, there was a delay of one month between the date when the samples were collected and the execution of the final simulations. During this month, the samples were stored in a freezer and were defrosted at least 2 times before the final round of measurements were made. Not only have the shells dried out; the live mussels and oysters also died, while the seaweed deteriorated through freezing and defrosting. Since the purpose of the experiment was to measure the spectral reflectance of the "shells" of the shellfish species using varying observation geometry, the death of the organisms did not hinder the experiment. However, the "drying out" of the shells, may have an effect on their spectra. Furthermore, when the samples were being measured, the high heat energy from the lamp caused the shells to open, as it is the reaction of the retained adductor muscle to open when subjected to high temperatures. This phenomenon not only contributed to the drying of shells, but also the possible spectral influence of the meat/tissue of the inside part of the shell.

B. Mechanism of the Goniometer

The goniometer used in the experiment was an instrument abandoned by a former PhD student. It was custom-made in Bulgaria. Unfortunately, the documentation regarding its proper use could not be found. Related literature (Coburn & Peddle, 2006; Biliouris et al., 2007) on the functionality of the said instrument was then used for reference. In Section 3.4.2., the instrument setup was described and the functionalities of the rings explained. However, considerable flaws still remain. First is regarding the construction of the goniometer. For example, the azimuthal ring of the goniometer was supported by four 3-cm legs. These legs were not leveled equally, making the instrument unsteady toward one side or another during the course of the experiment. One of the two movable rings where the lamp source was mounted on could not be placed directly overhead of the goniometer sphere. As mentioned in Section 3.4.2., this ring was tilted 30^{o}, when this should be in line or parallel with the ring holding the ASD. Additionally, there were not ready-made increments set on the rings—these increments were marked manually. As a result, deviations from the real 15^{o} increments may arise, particularly for the measurement between zenith angle 0 and 15^{o}.

The second mechanism-related flaw was in the set up of the various observation angles. For instance, the solar azimuth angle (SAA) was defined as the direction of the sensor towards marked increments on the wooden ring. The problem with this set up is that the accompanying viewing zenith and solar zenith angles no longer represent the true north, because the instrument is rotated at least three times towards a certain combination. Not to mention, the unevenness in the legs of the goniometer make it difficult to rotate and assure that the instrument is stable. In Biliouris et al. (2007), their custom-made goniometer allowed for azimuthal movement of the base ring. Such functionality was non-existent for the goniometer at hand, but azimuthal measurements were still attempted anyway. Also, the construction of the goniometer was done in a way that the ASD and the light source could only be adjusted within a range of 90^{o}. This means that at zenith, neither the ASD nor the light source could go further towards the other side of the 180^{o} sphere. This is also true for the case of the adjustments made for the VZAA.

C. Human Error

Lastly, the errors committed by the author are also identified, the most vital of which is the lack of repeated measurements (recordings) per unique combination. The same error was committed for the investigation of mussel and oyster spectra. In this particular case, though, repeated measurements for each combination (n=168) would have been impractical. The proposed solution then is to further limit the number of combinations that are achievable given the short time for analysis.

4.3.3. Discussion

The effect of varying observation geometries on the spectral distinctness of blue mussels and Japanese oysters was investigated. Four possible solar zenith angles (with corresponding relative solar azimuth angles) were chosen to represent the best illumination conditions for detecting reflectance spectra of shellfish species. Meanwhile, the viewing geometry of four sensors (2 multispectral and 2 hyperspectral) were considered and maximized in four possible viewing zenith angles for airborne and three for satellite sensors. Finally, six types of benthic cover were tested for a total of 168 unique combinations. In the procedure for selecting the best SZAs and SAAs, many factors were considered, aside from just the times of highest of solar radiation. Tidal levels were also considered, despite the fact that tidal levels vary from high to low tide twice in a day, and exact water levels are different everyday. A tidal pattern cannot be strictly produced but tidal information can be obtained in advance (see *Getijtabellen Nederland 2013* from Filo website). Information regarding tidal levels does not only suggest whether the mussel beds in question are submerged or exposed during image acquisition. Water waves can also affect spectral detection, as explained by Dekker et al. (2001): "the flight planning of airborne imaging spectroscopy campaigns needs to consider the solar zenith angles and azimuths that minimize imaging of sun glint effects of the water surface" (p. 326). Dekker et al. (2001) further explained that SZAs between 30^{o} to 60^{o} are optimal over water targets. The selection of SZAs and SAAs corresponding to noon time is also confirmed in Dekker et al. (2001), where flight time should be around 6-8 hours surrounding noon during the summer season in mid-latitude areas.

4.3. Image Pre-Processing

4.3.1. Assessment of Geometric Accuracy

The results showed an even more accurate reprojection compared to the image to image registration method. Assessment through the vector overlay showed an offset of only 0.5-1 pixel (1.5-3 meters) (see Figure 18). This accuracy was expected, since the projection of the vector shapefile and the geoTIFF were identical. To conclude, the use of the Match Existing File option was the simplest and quickest way to reproject images. Yet, even with the same coordinate system used between the vector shapefiles and the image, a perfect match cannot be assured.

Vector overlay showing harbor of Schiermonnikoog. Emphasis on building (dark pixels) position relative to vector overlay.

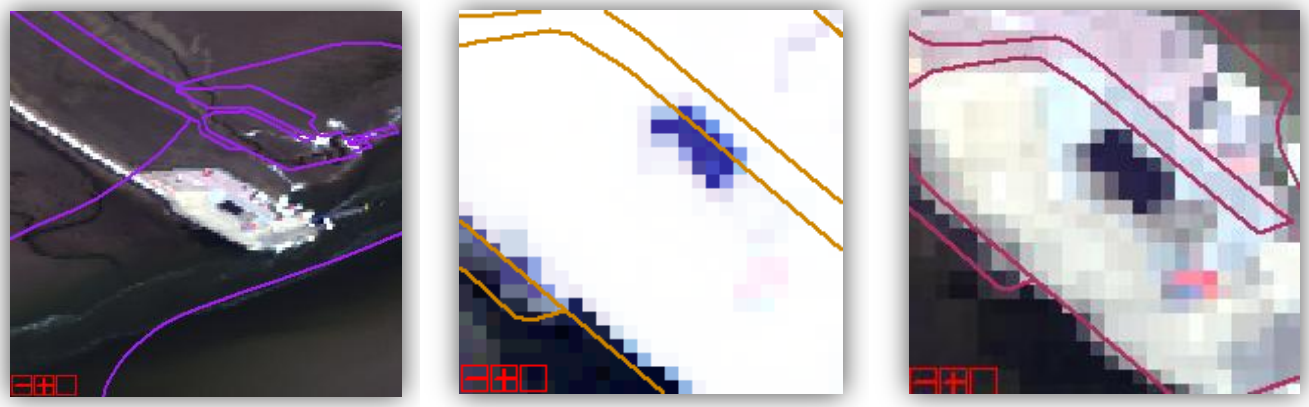

1. Result of Convert Map Projection **2. Result of Image to Image Registration** **3. Result of Match Existing File option**

Figure 18. Comparison of Reprojection Methods Used

4.3.2. Assessment of Atmospheric Corrections

A. Improvement in MODTRAN4 Settings

VITO re-processed the images using the original settings of Schiermonnikoog as basis. The AHS images of the two islands now have the same MODTRAN settings applied to them. It was important to assess the atmospheric parameters, as these are crucial, for instance, in giving the actual reflectance values in the VNIR region (Biesemans et al., 2007). To illustrate, the spectra of an agricultural land pixel in Ameland is seen in Figure 19. Slight differences in the VNIR region can be seen between the original image and the reprocessed image, particularly between 0.8-0.9 µm. The opportunity of having the HDF files at hand and getting the re-processing done, despite the fact that the imagery was meant to be supplied only in 2005-2006, was central in gaining confidence in the atmospheric quality of the images. It should be noted, however, that more appropriate corrections could have been implemented, such as tracing back the underlying reasons for the original values used (i.e., 25 km visibility for Ameland) or exploiting the availability of archived atmospheric data of weather stations near the islands (i.e., Terschelling for Ameland and Lauwerswoog for Schiermonnikoog).

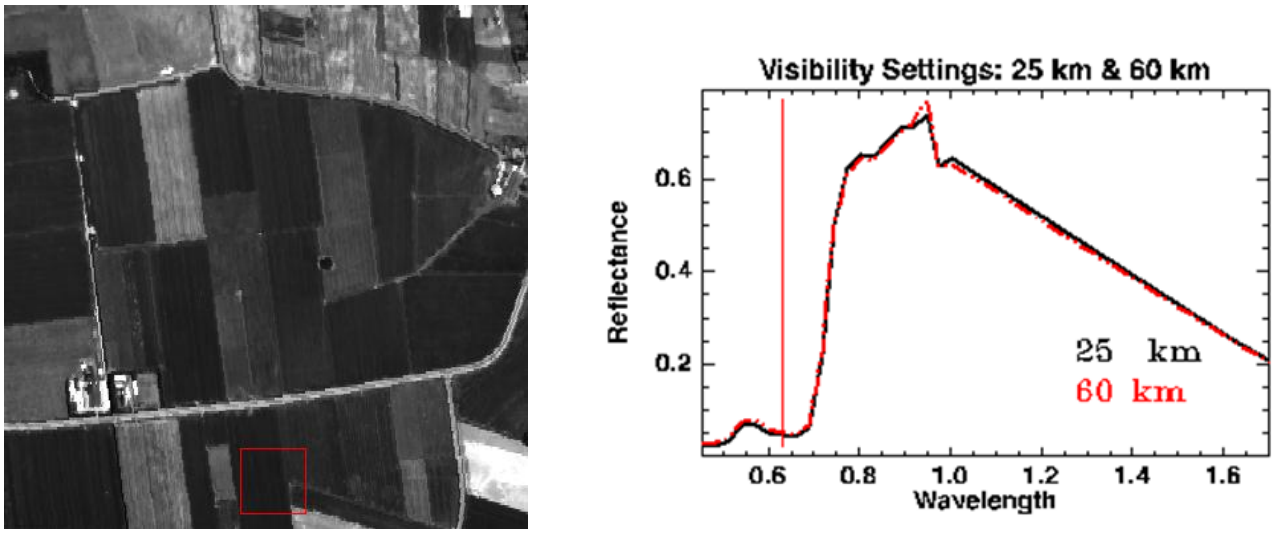

Agricultural land pixel (Band 1)

Figure 19. Results of MODTRAN4 Re-processing. Third Strip of Ameland.

B. Balancing of Reflectance Values using Band-Matching

In the implementation of the algorithm, the first input files were the first and second strips of each island. The output was the second strip with reflectance values adjusted to the first strip. In the following step, the third strip was adjusted to the values of the second trip. Strips 2 and 3 were normalized (strip 1 was not re-adjusted) for both Ameland and Schiermonnikoog. As a result, when these images were mosaicked, there was a smoother transition between the strips than compared to the original strips, as can be seen in the mosaic of 2 strips for Schiermonnikoog (see Figure 20).

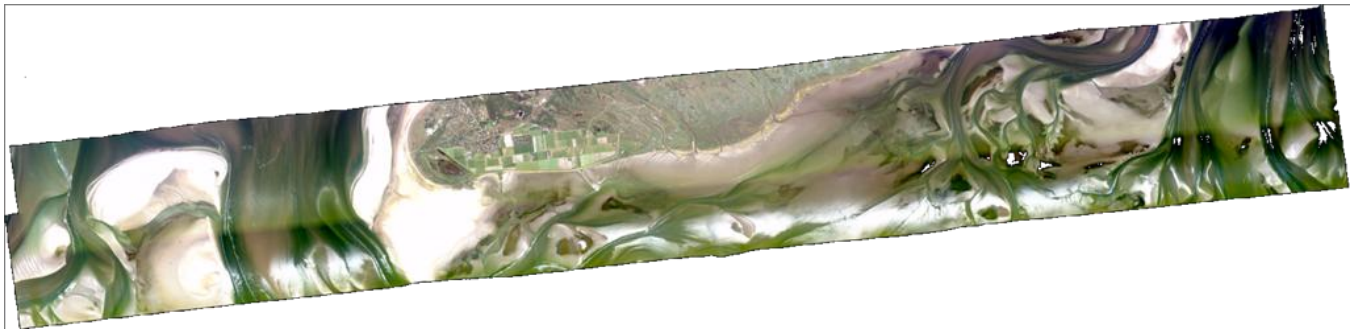

Figure 20. Results of the Band Matching Algorithm implemented on the AHS Imagery.

Recall that the band matching algorithm requires that the indicator for good matching between bands is an R^2 of 0.8 or higher. An R^2 less than that implies that either band do not regress well due to noise contained in the bands. Thus, these bands are flagged as bad bands and receive a value of 0 in the output normalized image. Table 9 presents the remaining good bands of each image after the algorithm implementation.

Table 9. Results of the Band Matching Algorithm

Image	Number of Good Bands	Retained bands ($R^2 \geq 0.8$)
WADAM_02	51	1-48, 50, 65-66
WADAM_03	36	1-3, 6-21, 66
WADSM_02	50	1-48, 65-66
WADSM_03	53	1-51, 65-66

The results show that most of the bands in the VNIR to SWIR regions (bands 1-48) were retained except for the third strip of Ameland (WADAM_03). Only two bands in the TIR region (bands 65-66) appear to regress well. Upon inspection of the output normalized images, however, one can see that the noise in the 2-2.0 µm region persisted. This was expected, as this feature was caused by a major system design issue (Gomez et al., 2007), one that cannot be corrected by a simple atmospheric correction. Nevertheless, the goal of the band matching algorithm was only to balance subtle, yet noticeable reflectance differences between flight strips, in order to produce a more color balanced mosaic, hence, comparable pixel reflectance values between strips.

5. Conclusion & Recommendations

The first component of the main objective of the research was to determine whether blue mussels and Japanese oysters were spectrally distinct and if such distinctness could be used to discriminate between the two shellfish species in airborne hyperspectral imagery. To achieve this, the spectral reflectance of mussels and oysters were investigated. It was found that the physicochemical properties of the shells of the two species caused them to have unique spectral signatures. Although the general shape of their reflectance were similar and comparable to other benthic cover types (e.g., seaweed), the application of continuum removal to their spectra as well as the results of the Mann-Whitney U test indicate that they do have diagnostic features that can be differentiated in 78 wavelengths (350-427 nm) at 0.01 level of significance. However, these bands do not coincide with the spectral range of the AHS hyperspectral image, which makes it difficult to discriminate between the two species using the said image.

The spectral reflectance of other benthic cover types present in the study area was also investigated. Through visual assessment, the spectra of shellfish were found to be similar in shape with each other as well as with seaweed (vegetation) spectra. Differences in their spectral features were also emphasized using continuum removal and through statistical tests. The results of the Mann-Whitney U showed that out of 15 benthic cover pairs, a maximum of 13 pairs were found to be statistically different ($p < 0.05$) in 67 wavelengths within the visible region (between 353 and 523 nm and at 701 nm). Only 28 of the 67 wavelengths coincided with the AHS spectral range. Wavelengths significant at 0.01 were more desired, and were found in the 12 out of 15 significant pairs. Of the 77 wavelengths, 74 were comparable with the AHS spectral range. Overall, it was found that the visible range holds the most potential for discriminating between mussel and oyster and among 6 benthic cover types.

The second component of the main objective of the research was to identify the requirements of hyperspectral imagery in detecting such species. This objective was only partly accomplished. The accomplishments include the critical appraisal of the image quality of the AHS hyperspectral datasets. Lessons could be learned from the assessment of system, radiometric, geometric, and atmospheric properties of the image. Additional information on hyperspectral as well as multispectral imaging of moisture-rich environments is needed. In conclusion, more knowledge on the spectral distinctness of mussels and oysters is needed and further analytical steps should be made in order to answer whether mussels and oysters can be spectrally discriminated in hyperspectral imagery.

5.1. Recommendations

For the investigation of mussel and oyster spectra:

- Explore also thermal reflectance
- Use wavelet smoothing techniques or spectral feature finding techniques
- Investigate further the bio-chemical composition of the shells through XRF, XRD, etc. Compare with other carbonate minerals such as aragonite
- Use the continuum removed spectra to test for statistical differences using the Mann-Whitney U test
- Apply Jeffries-Matusita separability test to significant bands resulting from the Mann-Whitney

For the simulation of observation geometries:

- Design an efficient goniometer
- Simulate other variables such as moisture and mixed benthic cover

For the requirements of hyperspectral images:

- Submit in-situ measurements for MODTRAN (i.e., water vapor content, visibility, etc.)
- Use newer AHS imagery (re-calibrated as of 2007) or other hyperspectral/multispectral imagery
- Take ground control points in the mudflats; use existing video location posts of Sovon
- Use available mussel bed shapefiles as possible validation data for image classification

6. References

Adler, H. H., & Kerr, P. F. (1962). Infrared study of aragonite and calcite. *The American Mineralogist, 47*, 700-717.

Anonymous. (2006). The shell. *Gireaud: Escargots, stevia & plantes pur tisane.* Retrieved August 1, 2012, from http://www.gireaud.net/us/coquille_us.htm

ASD Inc. (2008a). FieldSpec 3 user manual. Colorado, USA: ASD Inc.

ASD Inc. (2008b). ViewSpec Pro user manual. Colorado, USA: ASD Inc.

Banskota, A. (2006). *Estimating leaf area index of salt marsh vegetation using airborne hyperspectral data.* ITC, Enschede. Retrieved from http://www.itc.nl/library/papers_2006/msc/nrm/banskota.pdf

Barale, V., & Gade, M. (Eds.). (2008). *Remote sensing of the European seas*: Springer Science+Business Media B.V.

Biesemans, J., Sterckx, S., Knaeps, E., Vreys, K., Adriaensen, S., Hooy-berghs, J., . . . Nieke, J. (2007). *Image processing workflows for airborne remote sensing.* Paper presented at the 5th EARSeL SIG IS Workshop. Imaging Spectroscopy: Innovation in Environmental Research, Oud Sint-Jan, Bruges, Belgium.

Biliouris, D., Verstraeten, W., Dutré, P., Van Aardt, J., Muys, B., & Coppin, P. (2007). A Compact Laboratory Spectro-Goniometer (CLabSpeG) to Assess the BRDF of Materials. Presentation, Calibration and Implementation on Fagus sylvatica L. Leaves. *Sensors, 7*(9), 1846-1870.

Brockmann, C., & Stelzer, K. (2008). Optical remote sensing of intertidal flats. In V. Barale & M. Gade (Eds.), *Remote sensing of the European seas* (pp. 117-128). Germany, DE: Springer Verlag.

Büttger, H., Berg, T., & Nehls, G. (2010). *Evaluation of blue mussel beds in the North-Frisian Wadden Sea - according to the EU water framework directive and EU habitats directive.* Paper presented at the Science for Nature Conservation and Management: The Wadden Sea Ecosystem and EU Directives. Proceedings of the 12th International Scientific Wadden Sea Symposium, Wilhelmshaven, Germany.

Casal, G., Kutser, T., Domínguez-Gómez, J. A., Sánchez-Carnero, N., & Freire, J. (2011). Mapping benthic macroalgal communities in the coastal zone using CHRIS-PROBA mode 2 images. *Estuarine, Coastal and Shelf Science, 94*(3), 281-290. doi: 10.1016/j.ecss.2011.07.008

Clark, R. (1999). Chapter 1: Spectroscopy of rocks and minerals, and principles of spectroscopy. In A. N. Rencz (Ed.), *Manual of remote sensing* (Vol. 3, pp. 3-58). New York, NY: John Wiley and Sons.

Coburn, C. A., & Peddle, D. R. (2006). A low-cost field and laboratory goniometer system for estimating hyperspectral bidirectional reflectance. *Canadian Journal of Remote Sensing, 32*(3), 244-253.

Compere, E. L., Jr., & Bates, J. M. (1973). Determination of calcite: Aragonite ratios in mollusc shells by infrared spectra. *Limnology and Oceanography, 18*(2), 326-331.

Dekker, A. G., Brando, V., Anstee, J., Pinnel, N., Kutser, T., Hoogenboom, E., . . . Malthus, T. (2001). Imaging spectrometry of water. In F. D. Van der Meer & S. de Jong (Eds.), *Imaging spectrometry: Basic principles and prospective applications* (Vol. 4, pp. 307-359). Dordrecht, The Netherlands: Kluwer Academic Publishers.

Diederich, S. (2006). High survival and growth rates of introduced Pacific oysters may cause restrictions on habitat use by native mussels in the Wadden Sea. *Journal of Experimental Marine Biology and Ecology, 328*(2), 211-227. doi: 10.1016/j.jembe.2005.07.012

Ehlers, J. (1988). *Morphodynamics of the Wadden Sea*. Rotterdam: Balkema.

Ens, B. J. (2006). The conflict between shellfisheries and migratory waterbirds in the Dutch Wadden Sea. In G. C. Boere, C. A. Galbraith & D. A. Stroud (Eds.), *Waterbirds around the world* (pp. 806–811). Edinburgh: The Stationary Office.

Ens, B. J., Smaal, A. C., & De Vlas, J. (2004). The effects of shellfish fishery on the ecosystems of the Dutch Wadden Sea and Oosterschelde: Final report on the second phase of the scientific evaluation of the Dutch shellfish fishery policy (EVA II). Wageningen, the Netherlands.

Eriksson, B. K., van der Heide, T., van de Koppel, J., Piersma, T., van der Veer, H. W., & Olff, H. (2010). Major changes in the ecology of the Wadden Sea: Human impacts, ecosystem engineering and sediment dynamics. *Ecosystems, 13*(5), 752-764. doi: 10.1007/s10021-010-9352-3

Farson, D. (n.d.). Parts of mollusk shells. Retrieved August 1, 2012, from http://www.ehow.com/info_8091304_parts-mollusk-shells.html

Fey, F., Cremer, J., Dijkman, E., Jansen, J., Roupioz, L., Schmidt, A., & Dankers, N. (2009). *Development of analysis techniques for the use of aerial photography in the monitoring of intertidal mussel beds and oyster beds*. Wageningen, the Netherlands: IMARES.

Fey, F., Dankers, N., Meijboom, A., van Leeuwen, P., de Jong, M., Dijkman, E., & Cremer, J. (2011). *Ontwikkeling van enkele mosselbanken in de Nederlandse Waddenzee; situatie 2010*. Wageningen, the Netherlands: Insitute for Marine Resources & Ecosystem Studies (IMARES), Wageningen UR.

Gaffey, S. (1986). Spectral reflectance of carbonate minerals in the visible and near infrared (0.35-2.55 microns): Calcite, aragonite, and dolomite. *American Mineralogist, 71*, 151-162.

Gomez, J., de Miguel, E., de la Camara, O., & Fernandez-Renau, A. (2007). *Status of the INTA AHS sensor.* Paper presented at the 5th EARSeL SIG IS Workshop. Imaging Spectroscopy: Innovation in Environmental Research, Oud Sint-Jan, Bruges, Belgium.

Hennig, B. D., Cogan, B. C., & Bartsch, I. (2007). *Hyperspectral remote sensing and analysis of intertidal zones: A contribution to monitor coastal biodiversity.* Paper presented at the Proceedings of the First Geoinformatics Forum Salzburg 2007, Wichman Verlag, Heidelberg, Germany.

Herlyn, M. (2005). Quantitative assessment of intertidal blue mussel (Mytilus edulis L.) stocks: Combined methods of remote sensing, field investigation and sampling. *Journal of Sea Research, 53*(4), 243-253. doi: 10.1016/j.seares.2004.07.002

Herlyn, M., Millat, G., & Petersen, B. (2008). Documentation of sites of intertidal blue mussel (Mytilus edulis L.) beds of the Lower Saxonian Wadden Sea, southern North Sea (as of 2003) and the role of their structure for spatfall settlement. *Helgoland Marine Research, 62*(2), 177-188. doi: 10.1007/s10152-008-0106-y

Hochberg, E. J., & Atkinson, M. J. (2000). Spectral discrimination of coral reef benthic communities. *Coral Reefs, 19*(2), 164-171. doi: 10.1007/s003380000087

Hommersom, A., Wernand, M., Peters, S., & de Boer, J. (2010). A review on substances and processes relevant for optical remote sensing of extremely turbid marine areas, with a focus on the Wadden Sea. *Helgoland Marine Research, 64*(2), 75-92. doi: 10.1007/s10152-010-0191-6

Ibrahim, E., Adam, S., van der Wal, D., De Wever, A., Sabbe, K., Forster, R., & Monbaliu, J. (2009). Assessment of unsupervised classification techniques for intertidal sediments. *EARsel eProceedings, 8*(2), 158-179.

Jacob, D. E., Soldati, A. L., Wirth, R., Huth, J., Wehrmeister, U., & Hofmeister, W. (2008). Nanostructure, composition and mechanisms of bivalve shell growth. *Geochimica et Cosmochimica Acta, 72*(22), 5401-5415. doi: http://dx.doi.org/10.1016/j.gca.2008.08.019

Kumar, L., Skidmore, A. K., & Mutanga, O. (2010). Leaf level experiments to discriminate between eucalyptus species using high spectral resolution reflectance data: Use of derivatives, ratios and vegetation indices. *Geocarto International, 25*(4), 327-344. doi: 10.1080/10106040903505996

Laursen, K., Blew, J., Eskildsen, K., Günther, K., Hälterlein, B., Kleefstra, R., . . . Schrader, S. (2010). Migratory waterbirds in the Wadden Sea 1987-2008. *Wadden Sea Ecosystem* (Vol. 30). Wilhelmshaven, Germany: Common Wadden Sea Secretariat, Joint Monitoring Group of Migratory Birds in the Wadden Sea.

Leiper, I., Phinn, S., & Dekker, A. G. (2012). Spectral reflectance of coral reef benthos and substrate assemblages on Heron Reef, Australia. *International Journal of Remote Sensing, 33*(12), 3946-3965. doi: 10.1080/01431161.2011.637675

Lillesand, T. M., Kiefer, R. W., & Chipman, J. W. (2004). *Remote sensing and image interpretation* (5th ed.). New York, NY: Wiley & Sons.

Lowry, R. (2012). Subchapter 11a. The Mann-Whitney test. *Concepts and applications of inferential statistics*, from http://www.vassarstats.net/textbook/index.html

Millat, G., & Herlyn, M. (1999). Documentation of intertidal mussel bed (Mytilus edulis) sites at the coast of Lower Saxony. *Marine Biodiversity, 29*(0), 83-93. doi: 10.1007/bf03043129

Mulatu, H. (2006). *Land covers change detection using expert system and hyperspectral imagery in the island of Schiermonnikoog, the Netherlands.* ITC, Enschede. Retrieved from http://www.itc.nl/library/papers_2006/msc/gem/mulatu.pdf

National Oceanic and Atmospheric Administration. (n.d.). Solar calculator glossary Retrieved February 1, 2013, from http://www.esrl.noaa.gov/gmd/grad/solcalc/glossary.html#zenithangle

National Research Council Canada. (2005). Biology: An introductory guide to terms and function. Spectroscopy. Retrieved August 27, 2012, from http://www.nrc-cnrc.gc.ca/eng/education/biology/glossary.html

Nehls, G., Witte, S., Büttger, H., Dankers, N., Jansen, J., Millat, G., . . . Wehrmann, A. (2009). Beds of blue mussels and Pacific oysters. In H. Marencic & J. d. Vlas (Eds.), *Quality Status Report 2009. Wadden Sea Ecosystem* (Vol. 25). Wilhelmshaven, Germany.: Common Wadden Sea Secretariat, Trilateral Monitoring and Assessment Group.

Newell, R. I. E. (1989). *Species profiles: Life histories and environmental requirements of coastal fishes and invertebrates (North and Mid-Atlantic). Blue mussel (Biological report).* . USA: U.S. Fish and Wildlife Service and U.S. Army Corps of Engineers.

Nordsieck, R. (n.d.). Mussels and clams (Bivalvia). Retrieved August 1, 2012, from http://www.molluscs.at/bivalvia/index.html?/bivalvia/main.html

Pauley, G. B., van der Raay, B., & Troutt, D. (1988). *Species profiles: Life histories and environmental requirements of coastal fishes and invertebrates (Pacific Northwest). Pacific Oyster (Biological report).* . USA: U.S. Fish and Wildlife Service and U.S. Army Corps of Engineers.

Reise, K., Baptist, M., Burbridge, P., Dankers, N., Fischer, L., Flemming, B., . . . Smit, C. (2010). The Wadden Sea – A universally outstanding tidal wetland. *Wadden Sea Ecosystem* (Vol. 29). Wilhelmshaven, Germany: Common Wadden Sea Secretariat.

Reusen, I. (2005). AHS2005 flight campaign: VITO.

Ruddick, K., Lacroix, G., Lancelot, C., Nechad, B., Park, Y., Peters, S., & Van Mol, B. (2008). Optical remote sensing of the North Sea. In V. Barale & M. Gade (Eds.), *Remote sensing of the European seas* (pp. 79-90). Germany, DE: Springer Verlag.

Schill, S. R., Porter, D. E., Coen, L. D., Bushek, D., & Vincent, J. (2006). Development of an automated mapping technique for monitoring and managing shellfish distributions. Port Noris, NJ: NOAA/UNH Cooperative Institute for Coastal and Estuarine Environmental Technology (CICEET).

Schmidt, K. S., & Skidmore, A. K. (2003). Spectral discrimination of vegetation types in a coastal wetland. *Remote Sensing of Environment, 85*(1), 92-108. doi: 10.1016/s0034-4257(02)00196-7

Schmidt, K. S., Skidmore, A. K., Kloosterman, E. H., Oosten, H. v., Kumar, L., & Janssen, J. A. M. (2004). Mapping coastal vegetation using an expert system and hyperspectral imagery. *Photogrammetric Engineering and Remote Sensing, 70*(6), 703-715.

Smaal, A., Stralen, M., & Craeymeersch, J. (2005). Does the introduction of the Pacific Oyster *Crassostrea gigas* lead to species shifts in the Wadden Sea? In R. Dame & S. Olenin (Eds.), *The Comparative Roles of Suspension-Feeders in Ecosystems* (Vol. 47, pp. 277-289): Springer Netherlands.

Smith, A. (2009). *Lecture 4: Spectral indices and spectral separability*. For 570: Advanced remote sensing measurement methods. College of Natural Resources. University of Idaho. Retrieved from http://www.webpages.uidaho.edu/for570/pdfs/for570/Lecture%204_specindexand%20sep.pdf

Stoddard, P. (2003). Reconstruction of blue mussel beds using aerial photographs from 1989 and 2002 of the North Frisian Wadden Sea, Germany. Hockensbüll, Germany: BioConsult SH.

TeraScan. (2002). Angles - Computes satellite and solar viewing angles. *TeraScan functions* Retrieved February 1, 2013, from http://psbcw1.nesdis.noaa.gov/terascan/man1/angles.html

Trilateral Monitoring and Assessment Programme. (2011). TMAP monitoring handbook. Retrieved August 1, 2012, from http://www.waddensea-secretariat.org/TMAP/Handbook/guideline10.html

Tucker, C. (2009). Carol's cornwall. Retrieved August 21, 2012, from http://www.carolscornwall.com/On%20the%20Beach/Mollusc-Crassostrea%20gigas09-03-09.jpg

Ullah, S., Groen, T. A., Schlerf, M., Skidmore, A. K., Nieuwenhuis, W., & Vaiphasa, C. (2012). Using a genetic algorithm as an optimal band selector in the mid and thermal infrared (2.5–14 μm) to discriminate vegetation species. *Sensors, 12*(7), 8755-8769. doi: 10.3390/s120708755

Vahtmäe, E., & Kutser, T. (2007). Mapping bottom type and water depth in shallow coastal waters with satellite remote sensing. *Journal of Coastal Research, S1 50* (*Proceedings of the 9th International Coastal Symposium*), 185-189.

Vahtmäe, E., Kutser, T., Martin, G., & Kotta, J. (2006). Feasibility of hyperspectral remote sensing for mapping benthic macroalgal cover in turbid coastal waters—a Baltic Sea case study. *Remote Sensing of Environment, 101*(3), 342-351. doi: 10.1016/j.rse.2006.01.009

Vaiphasa, C. (2006). *Remote sensing techniques for mangrove mapping.* PhD Thesis, ITC, Enschede. Retrieved from http://intranet.itc.nl/papers/2006/phd/vaiphasa.pdf

van der Graaf, S., de Vlas, J., Herlyn, M., Voss, J., Heyer, K., & Drent, J. (2009). Macrozoobenthos. Thematic report No. 10. In H. Marencic & J. d. Vlas (Eds.), *Quality status report 2009. Wadden Sea ecosystem* (Vol. 25). Wilhelmshaven, Germany: Common Wadden Sea Secretariat.

van der Wal, D., Herman, P. M. J., Forster, R. M., Ysebaert, T., Rossi, F., Knaeps, E., . . . Ides, S. J. (2008). Distribution and dynamics of intertidal macrobenthos predicted from remote sensing: Response to microphytobenthos and environment. *Marine Ecology Progress Series, 367*, 57-72. doi: doi: 10.3354/meps07535

van Roomen, M., Laursen, K., van Turnhout, C., van Winden, E., Blew, J., Eskildsen, K., . . . Ens, B. J. (2012). Signals from the Wadden Sea: Population declines dominate among waterbirds depending on intertidal mudflats. *Ocean & Coastal Management*(0). doi: 10.1016/j.ocecoaman.2012.04.004

van Til, M., Bijlmer, A., & de Lange, R. (2004). Seasonal variability in spectral reflectance of coastal dune vegetation. *EARseL eProceedings, 3*(2), 154-165.

Venus, V., de Leeuw, J., & Skidmore, A. K. (2006). *Lecture notes: Statistics*. International Institute for Geo-Information Science and Earth Observation.

Verbeeten, T. (1999). *Wise use of the Wadden Sea? A study of policy-oriented learning Wadden Sea Newsletter 2000*. Universiteit Utrecht, FRW, Milieukunde en Omgevingsbeleid.

Verbeke, L., Scheerlinck, K., van Coillie, F., & de Wulf, R. (2006). Genetic algorithms for the segmentation and classification of hyperspectral imagery of Schiermonnikoog - The Netherlands. (L. o. F. M. a. S. I. T. D. o. F. a. W. Management., Trans.). Brugge, Belgium: Ghent University.

Wang, L., & Sousa, W. P. (2009). Distinguishing mangrove species with laboratory measurements of hyperspectral leaf reflectance. *International Journal of Remote Sensing, 30*(5), 1267-1281. doi: 10.1080/01431160802474014

. Wilcoxon rank sum and signed rank tests. (n.d.). *R Documentation Package stats version 2.15.0.* Retrieved December 17, 2012, from http://stat.ethz.ch/R-manual/R-patched/library/stats/html/wilcox.test.html

Wolff, W. J., Bakker, J. P., Laursen, K., & Reise, K. (2010). The Wadden Sea quality status report - synthesis report 2010. *Wadden Sea Ecosystem* (Vol. 29, pp. 25-74). Wilhelmshaven, Germany: Common Wadden Sea Secretariat.

7. Appendices

A. Photos of Benthic Cover Species

Samples of shells/seaweed inspected using the Contact Probe.

Japanese Oyster

Blue Mussel

Oyster covered with barnacles

Mussel covered with barnacles

Cockle

Seaweed

B. Sample Sheet of Solar Calculations

Use this spread sheet only if the local over pass time is known

Solar constant= 1367 <- Default solar radiation integrated for 0 to 20 micrometer range

Instructions

Set the yellow cells only. All calculations are done automatically.

	Input
Date	10-Sep-12
Local Time [hs]	14
Day [1->365]	253
Local Latitude [°]	53.45
Local Longitude [°]	6.15
Standard Meridian [°] [+ west]	-15.000

	Solar zenith angle [°]	Solar azimuth angle [°]	Solar altitude [°]	Solar declination [°]	Solar time [hs]	Extraterrestrial solar radiation [W/m2]
Output	**48.832**	**12.670**	**41.168**	**5.246**	**12.636**	**887**
June 19, 2005 (AHS images)						
1. Ameland 53.4 N, 5.56 E, 11:10 AM	**39.058**	**53.045**	**50.942**	**23.424**	**9.781**	**1027**
2. Ameland 53.4 N, 5.56 E, 11:29 AM	**36.889**	**46.897**	**53.111**	**23.424**	**10.098**	**1058**
3. Ameland 53.4 N, 5.56 E, 11:48 AM	**34.937**	**40.250**	**55.063**	**23.424**	**10.415**	**1084**
4. Schier 53.4 N, 6.38 E, 11:10 AM	**39.452**	**54.059**	**50.548**	**23.424**	**9.727**	**1021**
5. Schier 53.4 N, 6.38 E, 11:29 AM	**37.250**	**47.993**	**52.750**	**23.424**	**10.043**	**1053**
6. Schier 53.4 N, 6.38 E, 11:48 AM	**35.257**	**41.435**	**54.743**	**23.424**	**10.360**	**1080**
Fieldwork (Schiermonnikoog, 2 sites)						
Schier A						
*7. **Oct 24** 53.45 N, 6.15 E, 12:50 PM*	**65.054**	**-5.052**	**24.946**	**-11.482**	**11.688**	**583**
*8. **Oct 26** 53.45 N, 6.15 E, 1:30 PM*	**65.789**	**-5.763**	**24.211**	**-12.178**	**12.358**	**567**
Schier B						
*9. **Oct 27** 53.46 N, 6.18 E, 4:15 PM*	**76.988**	**-46.734**	**13.012**	**-12.522**	**15.108**	**312**

	Solar zenith angle [°]	Solar azimuth angle [°]	Solar altitude [°]	Solar declination [°]	Solar time [hs]	Extraterrestrial solar radiation [W/m2]
Output	**48.832**	**12.670**	**41.168**	**5.246**	**12.636**	**887**

Procedure

1. Choose 1 month to represent each season (exception for January and December, start & end of a year)
   - **Winter: January, December**
   - **Spring: April**
   - **Summer: June**
   - **Fall: October**
2. Choose 3 days per month for a 10-day interval
   - **10th, 20th, 30th of a month**
3. In Schier, there is a min of 7 and max of 16 sunlight hours in a year. Sunrise is between 4-8 am and Sunset between 4-9 pm
   - **I choose 2 hours before/after sunset/sunrise.**
   - **10:00 AM - 2:00 PM**

Finding the Range:						
Winter period (start of year)						
*10. **Jan 10** 53.45 N, 6.15 E, 10:00 AM*	**88.196**	**-47.634**	**1.804**	**-22.074**	**8.478**	**45**
*11. **Jan 10** 53.45 N, 6.15 E, 12:00 PM*	**78.070**	**-21.566**	**11.930**	**-22.074**	**10.478**	**292**
*12. **Jan 10** 53.45 N, 6.15 E, 2:00 PM*	**75.779**	**-6.848**	**14.221**	**-22.074**	**12.478**	**348**
*13. **Jan 20** 53.45 N, 6.15 E, 10:00 AM*	**87.033**	**-49.212**	**2.967**	**-20.300**	**8.418**	**73**
*14. **Jan 20** 53.45 N, 6.15 E, 12:00 PM*	**76.548**	**-22.830**	**13.452**	**-20.300**	**10.418**	**329**
*15. **Jan 20** 53.45 N, 6.15 E, 2:00 PM*	**73.950**	**-6.124**	**16.050**	**-20.300**	**12.418**	**391**
*16. **Jan 30** 53.45 N, 6.15 E, 10:00 AM*	**85.207**	**-50.903**	**4.793**	**-17.886**	**8.376**	**118**
*17. **Jan 30** 53.45 N, 6.15 E, 12:00 PM*	**74.361**	**-24.050**	**15.639**	**-17.886**	**10.376**	**380**
*18. **Jan 30** 53.45 N, 6.15 E, 2:00 PM*	**71.502**	**-5.665**	**18.498**	**-17.886**	**12.376**	**447**
Spring period						
*19. **April 10** 53.45 N, 6.15 E, 10:00 AM*	**61.707**	**61.830**	**28.293**	**7.655**	**8.563**	**645**
*20. **April 10** 53.45 N, 6.15 E, 12:00 PM*	**49.008**	**28.844**	**40.992**	**7.655**	**10.563**	**893**
*21. **April 10** 53.45 N, 6.15 E, 2:00 PM*	**46.304**	**11.612**	**43.696**	**7.655**	**12.563**	**941**
*22. **April 20** 53.45 N, 6.15 E, 10:00 AM*	**58.333**	**63.420**	**31.667**	**11.241**	**8.607**	**711**
*23. **April 20** 53.45 N, 6.15 E, 12:00 PM*	**45.391**	**29.439**	**44.609**	**11.241**	**10.607**	**951**
*24. **April 20** 53.45 N, 6.15 E, 2:00 PM*	**42.832**	**13.189**	**47.168**	**11.241**	**12.607**	**993**
*25. **April 30** 53.45 N, 6.15 E, 10:00 AM*	**55.343**	**65.120**	**34.657**	**14.522**	**8.638**	**766**

*26. **April 30** 53.45 N, 6.15 E, 12:00 PM*	**42.126**	**30.251**	**47.874**	**14.522**	**10.638**	**999**
*27. **April 30** 53.45 N, 6.15 E, 2:00 PM*	**39.654**	**14.607**	**50.346**	**14.522**	**12.638**	**1037**
	Solar zenith angle	**Solar azimuth angle**	**Solar altitude**	**Solar declination**	**Solar time**	**Extraterrestrial solar radiation [W/m2]**
	[°]	**[°]**	**[°]**	**[°]**	**[hs]**	
Output	**48.832**	**12.670**	**41.168**	**5.246**	**12.636**	**887**
Summer period						
*28. **June 10** 53.45 N, 6.15 E, 10:00 AM*						
*29. **June 10** 53.45 N, 6.15 E, 12:00 PM*	**48.761**	**71.851**	**41.239**	**22.959**	**8.607**	**874**
*30. **June 10** 53.45 N, 6.15 E, 2:00 PM*	**34.347**	**35.603**	**55.653**	**22.959**	**10.607**	**1094**
*31. **June 20** 53.45 N, 6.15 E, 10:00 AM*	**31.262**	**16.300**	**58.738**	**22.959**	**12.607**	**1133**
*32. **June 20** 53.45 N, 6.15 E, 12:00 PM*	**48.681**	**72.755**	**41.319**	**23.442**	**8.572**	**873**
*33. **June 20** 53.45 N, 6.15 E, 2:00 PM*	**34.087**	**36.728**	**55.913**	**23.442**	**10.572**	**1095**
*34. **June 30** 53.45 N, 6.15 E, 10:00 AM*	**30.701**	**15.539**	**59.299**	**23.442**	**12.572**	**1137**
*36. **June 30** 53.45 N, 6.15 E, 12:00 PM*	**49.149**	**73.100**	**40.851**	**23.236**	**8.536**	**864**
*37. **June 30** 53.45 N, 6.15 E, 2:00 PM*	**34.469**	**37.392**	**55.531**	**23.236**	**10.536**	**1089**
	30.821	**14.519**	**59.179**	**23.236**	**12.536**	**1135**
Fall period						
*38. **Oct 10** 53.45 N, 6.15 E, 10:00 AM*						
*39. **Oct 10** 53.45 N, 6.15 E, 12:00 PM*	**72.027**	**-50.776**	**17.973**	**-6.333**	**8.810**	**423**
*40. **Oct 10** 53.45 N, 6.15 E, 2:00 PM*	**61.655**	**-20.253**	**28.345**	**-6.333**	**10.810**	**651**
*41. **Oct 20** 53.45 N, 6.15 E, 10:00 AM*	**60.659**	**-13.884**	**29.341**	**-6.333**	**12.810**	**672**
*42. **Oct 20** 53.45 N, 6.15 E, 12:00 PM*	**75.089**	**-48.501**	**14.911**	**-10.055**	**8.846**	**355**
*43. **Oct 20** 53.45 N, 6.15 E, 2:00 PM*	**65.193**	**-18.830**	**24.807**	**-10.055**	**10.846**	**579**
*44. **Oct 30** 53.45 N, 6.15 E, 10:00 AM*	**64.418**	**-13.875**	**25.582**	**-10.055**	**12.846**	**595**
*45. **Oct 30** 53.45 N, 6.15 E, 12:00 PM*	**78.088**	**-46.673**	**11.912**	**-13.533**	**8.862**	**286**
*46. **Oct 30** 53.45 N, 6.15 E, 2:00 PM*	**68.561**	**-17.848**	**21.439**	**-13.533**	**10.862**	**507**
	67.895	**-13.587**	**22.105**	**-13.533**	**12.862**	**522**
Winter period (end of year)						
*47. **Dec 10** 53.45 N, 6.15 E 10:00 AM*						
*48. **Dec 10** 53.45 N, 6.15 E 12:00 PM*	**87.387**	**-44.435**	**2.613**	**-22.841**	**8.709**	**64**
*49. **Dec 10** 53.45 N, 6.15 E 2:00 PM*	**78.115**	**-18.197**	**11.885**	**-22.841**	**10.709**	**291**
*50. **Dec 20** 53.45 N, 6.15 E 10:00 AM*	**76.846**	**-10.059**	**13.154**	**-22.841**	**12.709**	**321**
*51. **Dec 20** 53.45 N, 6.15 E 12:00 PM*	**88.362**	**-45.098**	**1.638**	**-23.406**	**8.634**	**40**
*52. **Dec 20** 53.45 N, 6.15 E 2:00 PM*	**78.882**	**-19.110**	**11.118**	**-23.406**	**10.634**	**273**
*53. **Dec 30** 53.45 N, 6.15 E 10:00 AM*	**77.297**	**-8.941**	**12.703**	**-23.406**	**12.634**	**311**
*54. **Dec 30** 53.45 N, 6.15 E 12:00 PM*	**88.668**	**-46.141**	**1.332**	**-23.194**	**8.557**	**33**
*55. **Dec 30** 53.45 N, 6.15 E 2:00 PM*	**78.908**	**-20.216**	**11.092**	**-23.194**	**10.557**	**272**
	76.986	**-7.875**	**13.014**	**-23.194**	**12.557**	**319**

C. Benthic Cover Spectra for all Combinations of Observation Geometries

Mussel

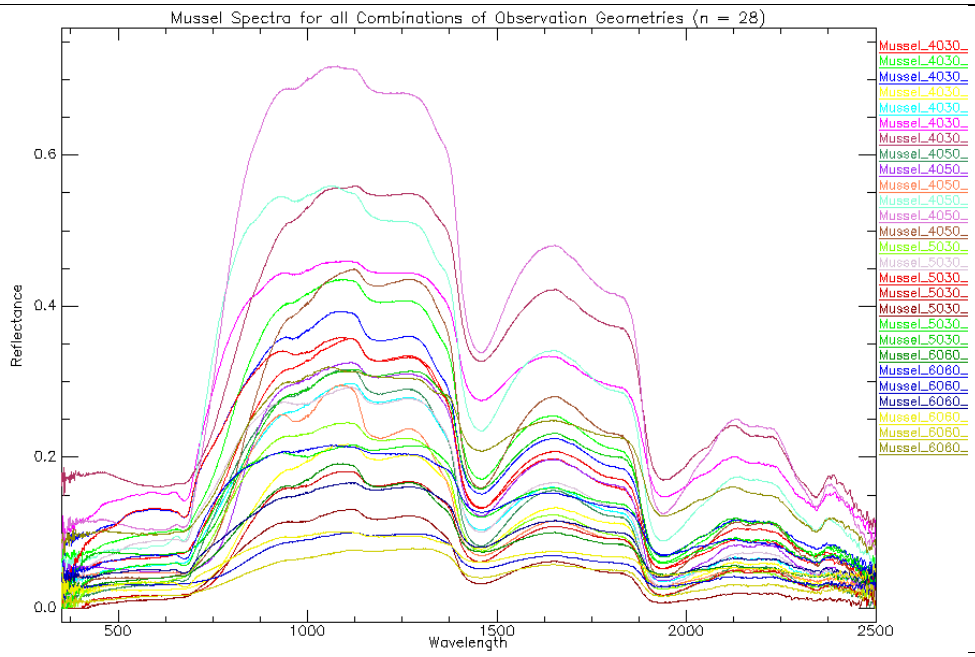

Seaweed

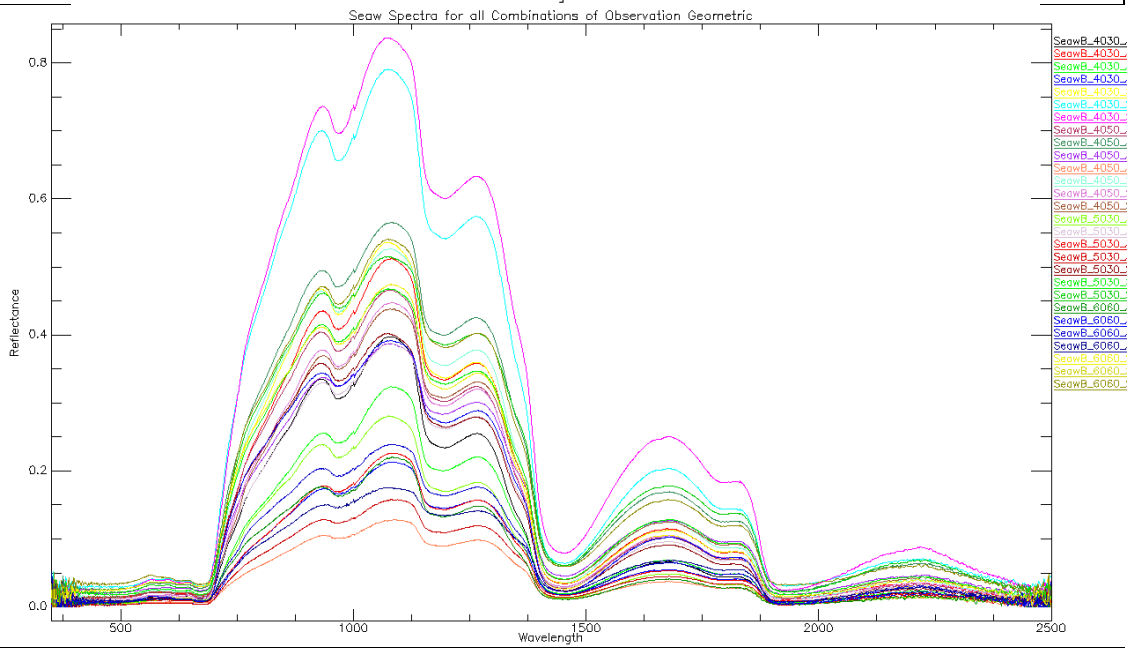

Mussel with barnacles	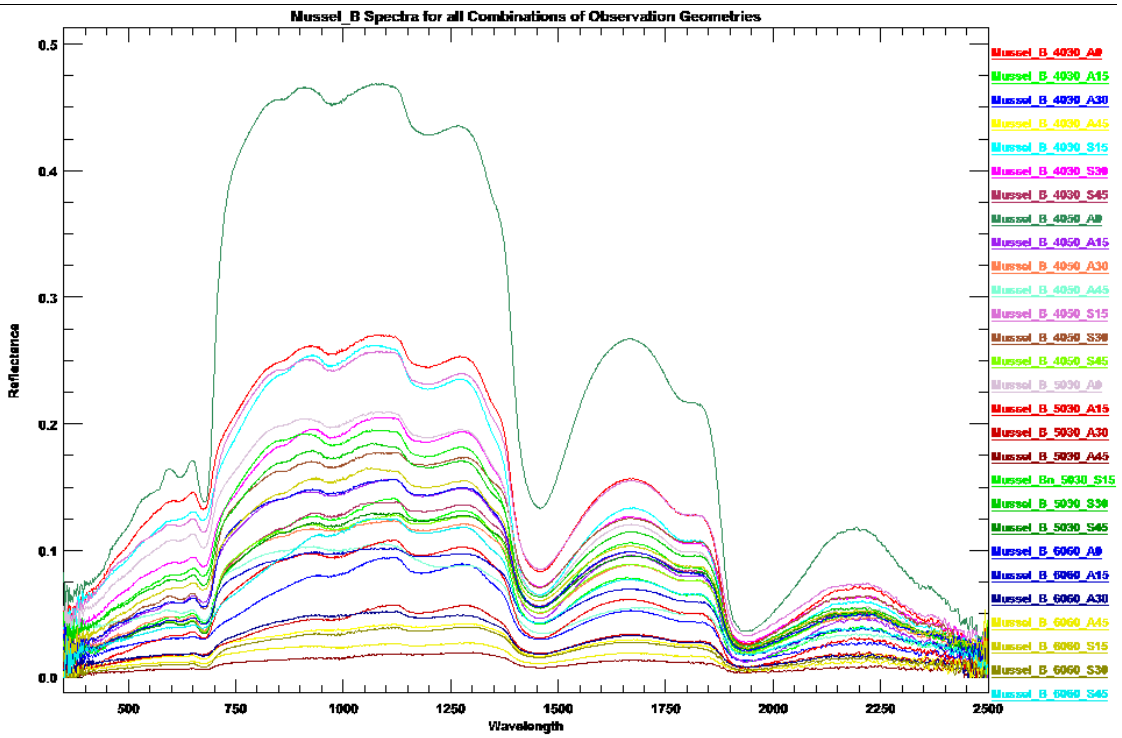
Oyster with barnacles